bioRxiv preprint doi: https://doi.org/10.1101/2021.05.10.443452; this version posted May 11, 2021. The copyright holder for this preprint (which was not certified by peer review) is the author/funder, who has granted bioRxiv a license to display the preprint in perpetuity. It is made available under aCC-BY-NC-ND 4.0 International license.

Title: Therapeutic reversal of prenatal pontine ID1 signaling in DIPG

Authors: Viveka Nand Yadav[1]*, Micah K. Harris[1], Dana Messinger[1], Chase Thomas[1], Jessica R. Cummings[1], Tao Yang[2], Rinette Woo[3], Robert Siddaway[4], Martin Burkert[5], Stefanie Stallard[1],Tingting Qin[7], Brendan Mullan[1], Ruby Siada[1], Ramya Ravindran[1], Michael Niculcea[1], Kevin F. Ginn[8], Melissa A.H. Gener[9], Kathleen Dorris[10], Nicholas A. Vitanza[11], Susanne V. Schmidt[12], Jasper Spitzer[12], Jiang Li[13], Mariella G. Filbin[13], Xuhong Cao[14], Maria G. Castro[15], Pedro R. Lowenstein[14], Rajen Mody[1], Arul Chinnaiyan[13], Pierre-Yves Desprez[3], Sean McAllister[3], Cynthia Hawkins[4], Sebastian M. Waszak[5,6], Sriram Venneti[1,14], and Carl Koschmann[1]*

Affiliations:
[1]Department of Pediatrics, Division of Pediatric Hematology-Oncology, University of Michigan Medical School; Ann Arbor, USA.
[2]Department of Neurology, University of Michigan Medical School; Ann Arbor, USA.
[3]Cancer Research, California Pacific Medical Center Research Institute; San Francisco, USA.
[4]Arthur and Sonia Labatt Brain Tumour Research Centre, Hospital for Sick Children, University of Toronto; Toronto, Canada.
[5]Centre for Molecular Medicine Norway (NCMM), Nordic EMBL Partnership, University of Oslo and Oslo University Hospital; Oslo, Norway.
[6]Department of Pediatric Research, Division of Pediatric and Adolescent Medicine, Rikshospitalet, Oslo University Hospital; Oslo, Norway.
[7]Department of Computational Medicine and Bioinformatics, University of Michigan Medical School; Ann Arbor, USA.
[8]Department of Pediatrics, Children's Mercy Kansas City; Kansas City, USA.
[9]Department of Pathology and Laboratory Medicine, Children's Mercy Kansas City; Kansas City, USA.
[10]Department of Pediatrics, University of Colorado School of Medicine; Aurora, USA.
[11]Department of Pediatrics, Seattle Children's; Seattle, USA.
[12]Institute of Innate Immunity, AG Immunogenomics, University Bonn; Bonn, Germany.
[13]Department of Pediatric Oncology, Dana-Farber Boston Children's Cancer and Blood Disorders Center; Boston, USA.
[14]Department of Pathology, University of Michigan Medical School; Ann Arbor, USA.
[15]Departments of Neurosurgery and Cell and Developmental Biology, University of Michigan Medical School; Ann Arbor, USA.

*Corresponding author. Viveka Nand Yadav[1], PhD (vyadav@med.umich.edu) and Carl J. Koschmann[1], MD (ckoschma@med.umich.edu). [1]Department of Pediatrics, Division of Pediatric Hematology-Oncology, University of Michigan Medical School, 1540 E Hospital Dr., Ann Arbor, Michigan 48109, USA (Tel: 734-936-9814; Fax: 734-232-8740

One Sentence Summary: The transcription factor ID1 is upregulated in a subset of DIPG tumor cells, and ID1-driven invasiveness is therapeutically targetable with CBD.

bioRxiv preprint doi: https://doi.org/10.1101/2021.05.10.443452; this version posted May 11, 2021. The copyright holder for this preprint (which was not certified by peer review) is the author/funder, who has granted bioRxiv a license to display the preprint in perpetuity. It is made available under aCC-BY-NC-ND 4.0 International license.

Abstract: Diffuse intrinsic pontine glioma (DIPG) is a highly aggressive brain tumor with rare survival beyond two years. This poor prognosis is largely due to the tumor's highly infiltrative and invasive nature. Previous reports demonstrate upregulation of the transcription factor ID1 with H3K27M and *ACVR1* mutations, but this has not been confirmed in human tumors or therapeutically targeted. We developed an in utero electroporation (IUE) murine H3K27M-driven tumor model, which demonstrates increased ID1 expression in H3K27M- and *ACVR1*-mutated tumor cells. In human tumors, elevated ID1 expression is associated with H3K27M/*ACVR1*-mutation, brainstem location, and reduced survival. The *ID1* promoter demonstrates a similar active epigenetic state in H3K27M tumor cells and murine prenatal hindbrain cells. In the developing human brain, ID1 is expressed highest in oligo/astrocyte-precursor cells (OAPCs). These $ID1^{+}$/$SPARCL1^{+}$ cells share a transcriptional program with astrocyte-like (AC-like) DIPG cells, and demonstrate upregulation of gene sets involved with regulation of cell migration. Both genetic and pharmacologic [cannabidiol (CBD)] suppression of ID1 results in decreased DIPG cell invasion/migration in vitro and invasion/tumor growth in multiple in vivo models. CBD reduces proliferation through reactive oxygen species (ROS) production at low micromolar concentrations, which we found to be achievable in the murine brainstem. Further, pediatric high-grade glioma patients treated off-trial with CBD (n=15) demonstrate tumor ID1 reduction and improved overall survival compared to historical controls. Our study identifies that *ID1* is upregulated in DIPG through reactivation of a developmental OAPC transcriptional state, and ID1-driven invasiveness of DIPG is therapeutically targetable with CBD.

bioRxiv preprint doi: https://doi.org/10.1101/2021.05.10.443452; this version posted May 11, 2021. The copyright holder for this preprint (which was not certified by peer review) is the author/funder, who has granted bioRxiv a license to display the preprint in perpetuity. It is made available under aCC-BY-NC-ND 4.0 International license.

INTRODUCTION

Diffuse intrinsic pontine glioma (DIPG) is a lethal pediatric brain tumor that originates in the pons (*1*). With a median survival of 10-11 months, DIPG remains the most aggressive primary brain tumor in children (*2*). Standard of care consists of palliative radiation, and experimental chemotherapies have yet to demonstrate benefit beyond radiation (*2*). Even with the advent of precision-based medicine, clinical trials targeting specific molecular targets are lacking, highlighting the need to identify novel therapeutic targets in DIPG.

As many as 80% of DIPGs harbor mutations in histone H3, which leads to a lysine-to-methionine substitution (H3K27M) in *H3.3A* (*H3F3A*) and *H3C2* (*HIST1H3B*) (*1, 3*). H3K27M is now understood to define a distinct clinical and biological subgroup in DIPG, and is associated with a worse prognosis (*4*). The H3K27M mutation represses the polycomb repressive complex 2 (PRC2), resulting in global reduction of H3K27me3 (with focal gains) (*5*) and global increases in acetylation of H3K27 (H3K27ac), associated with upregulation of tumor-driving genes (*6, 7*).

Basic helix-loop-helix (bHLH) transcription factors are key regulators of tissue and lineage-specific gene expression, and constitutive expression of Inhibitor of DNA binding (ID) proteins have been shown to inhibit the differentiation of multiple tissues (*8*). ID proteins dimerize with bHLH transcription factors, preventing DNA binding (*9*). Overexpression of the Inhibitor of DNA binding 1 (*ID1*) gene has been tied to the pathogenesis of multiple human cancers (*10-12*). A role for ID1 in DIPG has been proposed, based on its downstream association with activin A receptor type 1 (ACVR1) signaling, which is recurrently mutated/activated in 25% of human DIPGs (*13-15*). Germline *ACVR1* mutations in the congenital malformation syndrome fibrodysplasia ossificans progressiva (FOP) activate the bone morphogenetic protein (BMP) signaling pathway, through enhanced recruitment and phosphorylation of SMAD1/5/8, which in

bioRxiv preprint doi: https://doi.org/10.1101/2021.05.10.443452; this version posted May 11, 2021. The copyright holder for this preprint (which was not certified by peer review) is the author/funder, who has granted bioRxiv a license to display the preprint in perpetuity. It is made available under aCC-BY-NC-ND 4.0 International license.

turn increases ID1 expression (*16*). Prior studies have shown K27M and *ACVR1* to upregulate *ID1* in cultured human astrocytes and murine models of DIPG (*13, 14*). ID1 has been shown to drive an invasive tumor phenotype in multiple solid tumors (*10, 11*). Invasion into normal pontine tissue is a pathognomonic feature of DIPG, but its regulation remains poorly understood. Further, analysis of ID1 in human DIPG, and its regulation and targetability, have not been previously investigated.

In the present study, we show that human DIPGs demonstrate epigenetic activation and increased expression of ID1, influenced by H3K27M and *ACVR1* mutational status and brain location. This epigenetic activation mimics ID1 regulation in the developing human and murine prenatal pons. Genetic knockdown and pharmacologic [cannabidiol (CBD)] inhibition of ID1 decreases invasion and migration and improves survival in multiple preclinical DIPG models and human patients. These findings represent an exciting new direction for understanding the regulation and targetability of invasion in DIPG, with broad implications for therapeutic targeting of solid tumors with ID1 up-regulation.

RESULTS

Increased ID1 expression with H3K27M and ACVR1 mutations in murine DIPG tumor model

We first sought to confirm whether ID1 expression is affected by the presence of H3K27M and *ACVR1* mutations. We adopted an in utero electroporation (IUE) model of pediatric high-grade glioma (pHGG), as previously described by our group (*17*). Mice developed tumors [mutant TP53, mutant PDGFRA (D842V) with *H3.3A* K27M mutation ("PPK") or *H3.3A* wildtype ("PPW")] via plasmid injection into the lateral ventricles of E13.5 embryonic CD1

bioRxiv preprint doi: https://doi.org/10.1101/2021.05.10.443452; this version posted May 11, 2021. The copyright holder for this preprint (which was not certified by peer review) is the author/funder, who has granted bioRxiv a license to display the preprint in perpetuity. It is made available under aCC-BY-NC-ND 4.0 International license.

mice (Fig. 1A-B). Transfection efficiency and tumor growth/size were monitored using in vivo bioluminescence imaging, and primary neurosphere cell cultures were generated for each group by tumor dissociation (Fig. 1B). Survival analysis revealed that PPK mice (n=15) had significantly reduced survival compared to their H3$^{\text{Wildtype (WT)}}$ counterparts (PPW; n=10) (Fig. 1C). Additionally, immunohistochemistry (IHC) and western blot analyses of murine tumors showed tumor-specific expression of H3K27M and global loss of H3K27me3 expression, a salient feature expected in H3K27M-mutant DIPG tumors (Fig. 1D-E) (*18*). Importantly, ID1 expression was elevated in PPK tumors compared to PPW (Fig. 1E). In order to determine the impact of *ACVR1* mutation on ID1 expression in DIPG, we introduced *ACVR1* mutation via lentiviral (LV) transduction into PPK tumor cells and primary *H3.3A* K27M/*ACVR1*^{WT} human DIPG cells (DIPGXIIIp). Western blot analysis revealed increased ID1 expression and SMAD activation with the introduction of *ACVR1* mutation in both PPK and DIPGXIIIp tumor cells (Fig. 1F), consistent with previous reports (*13, 14*).

ID1 expression increased in human DIPG and associated with lower overall survival

We next assessed the impact of H3K27M (*H3.3A* or *H3C2*) and *ACVR1* mutations on *ID1* expression in DIPG and non-brainstem pHGG. Whole transcriptome sequencing was performed on 34 DIPG and 18 normal post-mortem brain tissue specimens taken from a single institutional cohort (Sick Kids, Toronto). Compared to normal brain (cortex), DIPG tissue showed significantly higher *ID1* expression (Fig. 1G). Single cell RNA-sequencing (scRNA-seq) data from H3K27M-mutant DIPG tumors [Dana-Farber Cancer Institute (DFCI) cohort (*19*)] confirmed that malignant cells display significantly higher *ID1* expression compared to nonmalignant cells within these tumors (Fig. S1A). ScRNA-seq data from H3K27M-pHGG

bioRxiv preprint doi: https://doi.org/10.1101/2021.05.10.443452; this version posted May 11, 2021. The copyright holder for this preprint (which was not certified by peer review) is the author/funder, who has granted bioRxiv a license to display the preprint in perpetuity. It is made available under aCC-BY-NC-ND 4.0 International license.

patients (n=14) revealed higher *ID1* expression in pontine H3K27M-DIPG cells compared to thalamic and cortical pHGG tumors (Fig. 1H). This was confirmed in bulk RNA-seq [ICR cohort (Institute for Cancer Research), n=198 (*20*)], in which brainstem pHGG tumors (DIPG) showed significantly higher *ID1* expression than cortical pHGGs (Fig. 1I). High *ID1* expression has been linked to lower overall survival (OS) in multiple cancers (*21*). Indeed, DIPG patients with higher bulk *ID1* expression (ICR cohort) have lower OS (Fig. 1J). These data support that ID1 is involved in the pathogenesis of human DIPG.

ID1 expression influenced by H3 and ACVR1 mutational status in human DIPG

Introduction of the recurrent mutations *H3.3A* K27M and *ACVR1* have been shown to increase *ID1* expression in cultured astrocytes (*13, 14*), consistent with findings in our IUE tumor model (Fig. 1E). Analysis of bulk tumor RNA-seq (ICR cohort) revealed that *ID1* expression is significantly increased in pHGGs harboring H3K27M (*H3.3A* or *H3C2*) compared to $H3^{WT}$ and H3G34R tumors (Fig. 1K) (*20*). *ACVR1*-mutant tumors (Fig. 1L) and those with co-mutation (H3K27M and *ACVR1*, Fig. 1M) have significantly higher *ID1* expression compared to WT tumors. Interestingly, in scRNA-seq data (DFCI cohort), elevated *ID1* expression is seen in a higher proportion of malignant cells within pontine H3K27M tumors (n=4; 35-69%) in comparison to thalamic H3K27M tumors (n=2; 6-9%) (Fig. S1B). Taken together, these data support that *ID1* expression in pHGG is driven by both mutational status of H3 and *ACVR1* and regional (anatomic) influences.

Epigenetic state of ID1 loci in H3K27M tumor cells and murine prenatal hindbrain cells

bioRxiv preprint doi: https://doi.org/10.1101/2021.05.10.443452; this version posted May 11, 2021. The copyright holder for this preprint (which was not certified by peer review) is the author/funder, who has granted bioRxiv a license to display the preprint in perpetuity. It is made available under aCC-BY-NC-ND 4.0 International license.

In patients with germline *ACVR1*-mutant FOP or DIPG tumors with somatic *ACVR1* mutations, ID1 expression is activated by BMP signaling (*15, 22*). However, the mechanism of H3K27M mutation promoting increased ID1 expression is less understood. We assessed whether H3K27ac and H3K27me3 marks at regulatory regions of the *ID1* gene could be contributing to the increased *ID1* expression observed in human DIPG. Quantitative PCR (qPCR) demonstrated *ID1* expression to be higher in H3K27M and *ACVR1*-mutant DIPG autopsy samples (n=4 tumor sites) compared to H3WT/*ACVR1*^{WT} DIPG tissue (n=6 tumor sites) and normal brain tissue samples (n=4 sites) Fig. 2B and S2A-C). ChIP-Seq at the ID1 gene loci on normal adolescent pontine (n=1), H3^{WT} DIPG (n=1) and H3K27M DIPG (n=4) samples revealed a marked increase in H3K27ac deposition at *ID1* gene body elements in H3K27M DIPG tumor tissue compared to H3^{WT} DIPG tumor and normal pontine tissue, with minimal H3K27me3 marks across the ID1 loci in all tissue types (Fig. 2C). Subsequent ChIP-qPCR for quantification (primers in Supplemental Table 1) demonstrated significantly elevated H3K27ac at predicted promotor and gene body regions of the ID1 locus compared to H3WT/ACVR1^{WT} DIPG tumor samples (Fig. 2D). Decreased H3K27me3 was also observed, though this was only significant at one of the predicted promotor regions between H3K27M/ACVR1^{MUT} and H3^{WT}/ACVR1^{WT} DIPG sample groups (Fig. 2E). Taken together, however, the effects of these changes in H3K27ac and K3K27me3 marks correspond with H3K27M-mutant samples being epigenetically activated for ID1 expression.

While brainstem tumors broadly show increased *ID1* expression compared to normal brain, we noted differences in expression by qPCR between multi-focal autopsy samples. Expanded multi-focal (n=6) bulk RNA-sequencing of a single H3K27M/*ACVR1*-mutant DIPG patient (UMPED12) confirmed varying levels of *ID1* expression across different regions of the

bioRxiv preprint doi: https://doi.org/10.1101/2021.05.10.443452; this version posted May 11, 2021. The copyright holder for this preprint (which was not certified by peer review) is the author/funder, who has granted bioRxiv a license to display the preprint in perpetuity. It is made available under aCC-BY-NC-ND 4.0 International license.

tumor (Fig. 2F). This finding led us to analyze scRNA-seq in order to determine whether a specific malignant cell subpopulation could be contributing to the increased *ID1* expression seen in DIPG. Assessment of *ID1* expression across all malignant cell types in DIPG cells from four patients showed that *ID1* is most highly expressed in DIPG cells with an astrocytic differentiation program [“AC-like cells” (*19*)], followed by oligodendrocyte precursor cell-like (“OPC-like”) cells (Fig. 2G and S3A). OPC-like cells are known to constitute the majority of cycling cells in DIPG (*19*). Previous analysis showed that nearly all cycling DIPG cells have an OPC-like phenotype (*19*) and we observed higher levels of *ID1* expression in cycling compared to non-cycling cells (Fig. S3B).

Single-cell transcriptional analysis of ID1^{+} cells in human developing brain and H3K27M tumors

Anatomic location and developmental context strongly influence the formation of many pediatric tumors, including DIPG. We next assessed *ID1* expression and histone modifications across pre- and post-natal mouse brain developmental stages. RNA in-situ hybridization data (Allen Brain Atlas) demonstrated *ID1* to be highest expressed in the developing prenatal mouse hindbrain (including the developing pons) compared to forebrain or midbrain, with minimal *ID1* expression throughout the entire postnatal mouse brain (Fig. 3A-B and S4). In E15.5 mouse brains, ENCODE data (*23, 24*) revealed H3K27ac to be elevated at *ID1* enhancer sites in the hindbrain compared to midbrain and forebrain (Fig. S5A-B).

Analysis of developing human (*25*) and mouse (*26*) brain scRNA-seq data showed that *ID1* expression peaks at gestational week (GW) 12-22 in the human pons (Fig. 3C) and early postnatal mouse pons (P0; Fig. S6-S7), and is most highly expressed in astrocytes. *ID1*

bioRxiv preprint doi: https://doi.org/10.1101/2021.05.10.443452; this version posted May 11, 2021. The copyright holder for this preprint (which was not certified by peer review) is the author/funder, who has granted bioRxiv a license to display the preprint in perpetuity. It is made available under aCC-BY-NC-ND 4.0 International license.

expression is also high in human endothelial cells, consistent with previous data (Fig. 3C) (*27*). IHC analyses of pre- and post-natal brains confirmed elevated ID1 in the murine embryonic brain (E18; Fig. 3D) and human GW 20.5 brain (Fig. 3E) in subventricular regions lining the 4th ventricle, compared to all postnatal brain locations.

We next sought to assess whether *ID1*$^{+}$ sub-populations of malignant DIPG cells share a transcriptional program with *ID1*$^{+}$ developing brain cells. Interestingly, AC-like cells from all four DIPG tumors show the strongest overlap with the transcriptional program of the recently defined OAPC cell population (*28*) in the developing human brain (Fig. 3F). The OAPC program was not enriched in OPC-like cells in any of the four DIPG tumors (Fig. 3F). OAPCs are present primarily in the outer subventricular zone during the neurogenesis-to-gliogenesis switch period and express both astrocyte (GFAP) and oligodendrocyte (OLIG1, OLIG2) marker genes as well as SPARCL1, which is involved in regulation of cell adhesion (*28*). We found *ID1* to be a marker gene for both AC-like DIPG cells and OAPCs. Immunofluorescence of human H3K27M-DIPG samples revealed co-localization of ID1 and SPARCL1 expression in sub-populations of cells (Fig. 3G). Assessment of SPARCL1 expression across all malignant cell types in DIPG cells from four patients showed that SPARCL1 is most highly expressed in AC-like DIPG cells. Importantly, AC-like DIPG cells demonstrate enrichment of gene sets involved in regulation of cell adhesion and migration (Fig. S9), further implicating the potential role of *ID1*$^{+}$ AC-like cells in the regulation of DIPG tumor cell invasion and migration.

Impact of genetic and pharmacologic knockdown of ID1 on invasion and migration

To examine the phenotypic impact of *ID1* in human DIPG cells, a patient-derived DIPG cell culture with *H3.3A* K27M and *ACVR1* mutation (DIPG007) was lentivirally-transduced with

bioRxiv preprint doi: https://doi.org/10.1101/2021.05.10.443452; this version posted May 11, 2021. The copyright holder for this preprint (which was not certified by peer review) is the author/funder, who has granted bioRxiv a license to display the preprint in perpetuity. It is made available under aCC-BY-NC-ND 4.0 International license.

ID1-targeting shRNA or scrambled shRNA control (Fig. 4A). *ID1* knockdown (shRNA-64) resulted in reduced SPARCL1 expression in DIPG007 cells by western blot, further implicating the role of *ID1* in the regulation of this OAPC/AC-like cell marker gene (Fig. 4B). *ID1* knockdown significantly reduced DIPG007 invasion (Fig. 4C) and migration, as measured by scratch assay percent wound closure (Fig. 4D-E). In comparison, invasion and migration of human embryonic kidney cell line HEK293 was not affected upon *ID1* knockdown (Fig. S10A-C).

A few compounds that reduce *ID1* expression include Cannabidiol (CBD), Pimozide, 2-Methoxyestradiol and MK615 (*29-31*). Of these, CBD is the most studied, clinically available and CNS-penetrant agent (*32, 33*). CBD is the non-psychoactive compound found in *Cannabis sativa* (*34*). CBD has wide-ranging impacts on cellular behavior, including the ability to downregulate expression of *ID1* and to inhibit invasion in multiple pre-clinical cancer models (*12, 35-37*). Based on these studies, we sought to investigate the targeting of ID1 in DIPG through use of CBD. Treatment of human DIPG007 and mouse PPK cells with CBD reduced *ID1* expression (Fig. 4F) and cell viability (Fig. 4G), with an IC_{50} of 2.4 and 2.5 μM, respectively. We also treated two additional human DIPG cell cultures with H3K27M/ACVR1^{WT} status, DIPGXIIIp and PBT-29, with CBD, and found reductions in cell viability at an IC_{50} of 6.8 and 7.2 μM, respectively (Fig. S11A-B). Additionally, CBD treatment resulted in significantly reduced invasion and migration of human DIPG007 cells (Fig. 4H-I and S12A-B) and human PBT-29 cells (Fig. S12C-F) in the 5-10 uM range.

CBD has been reported to increase intracellular levels of reactive oxygen species (ROS) (*38*). In line with this, our data reveal that DIPG007 cells treated with CBD show a dose dependent increase in ROS levels (Fig. 4J). Additional treatment with α-tocopherol (TOC), a

bioRxiv preprint doi: https://doi.org/10.1101/2021.05.10.443452; this version posted May 11, 2021. The copyright holder for this preprint (which was not certified by peer review) is the author/funder, who has granted bioRxiv a license to display the preprint in perpetuity. It is made available under aCC-BY-NC-ND 4.0 International license.

ROS scavenger (*37, 38*), severely restricted the ability of CBD to inhibit proliferation of DIPG007 cells (Fig. 4K).

Genetic knockdown of ID1 in IUE murine model

In order to assess whether *ID1* suppression would impede tumor growth in PPK mice, we developed a PBase-responsive ID1-shRNA plasmid and scrambled short hairpin ("sh-control"). PPK-ShID1 mice exhibited significantly prolonged survival when compared to PPK-Sh-control mice (Fig. 5A). PPK-ShID1 mice demonstrated significantly-extended median survival (p=0.01) and reduced luminescent tumor signals when compared to control mice (Fig. 5B-C). IHC analysis of moribund tumors demonstrated reductions in ID1 and Ki67 expression (Fig. 5D-E) in PPK-ShID1 tumors. PPK-ShID1 tumors also exhibited more distinct tumor borders (e.g. reduced tumor invasion into normal brain) in vivo (Fig. 5F). Implantation of DIPG007 cells with ShID1 (or control) into the brainstem of NSG mice also demonstrated reduced pace of luminescent growth (Fig. S13A-C), although this did not affect overall tumor survival. These data indicate that genetic ID1 knockdown inhibits tumor growth in vivo and reduces tumor invasion and proliferation.

Pharmacological inhibition of ID1 with Cannabidiol (CBD) in IUE murine model

We next proceeded to our IUE PPK murine model to assess the impact of CBD in vivo. We performed daily treatment with CBD (15 mg/kg), or vehicle control. CBD treatment significantly improved median survival compared to vehicle control (Fig. 6A). Moribund tumors treated with CBD showed reductions in ID1 and Ki67 expression following CBD treatment (Fig. 6B-C). Additionally, CBD-treated tumors displayed reduced invasiveness of tumor cells

bioRxiv preprint doi: https://doi.org/10.1101/2021.05.10.443452; this version posted May 11, 2021. The copyright holder for this preprint (which was not certified by peer review) is the author/funder, who has granted bioRxiv a license to display the preprint in perpetuity. It is made available under aCC-BY-NC-ND 4.0 International license.

compared to vehicle-treated mice (Fig. S14). Both genetic (ShID1) and pharmacologic (CBD) knockdown of ID1 in murine models resulted in reduced tumor infiltration into the contralateral hippocampus compared to controls (Fig. 6D). These data indicate that CBD reduces ID1 expression and tumor invasion and significantly improves survival of H3K27M-mutant tumors in vivo.

We next assed the pharmacokinetic distribution of CBD in normal brain and brain tumor cells (Fig. 6E-F). After IP administration of a 45 mg/kg dose of CBD, we noted a similar peak concentration of CBD in the brainstem and plasma (6 and 7 uM, respectively) (Fig. 6G), which is above the previously determined IC_{50} dose of CBD in our DIPG cells. At 2 hours, we found equivalent doses of CBD in plasma, brain and brain tumor samples in our PPK model (Fig. 6H).

CBD treatment in pHGG patients

CBD is increasingly popular as an off-trial, non-prescribed therapy among patients with pHGG (*39*), including DIPG. However, its use remains controversial as no preclinical efficacy, mechanistic data, dosing or clinical studies of CBD in DIPG have been performed. We gathered patient-reported CBD dosing from families of pHGG patients at two institutions (n=15 total, n=8 DIPG, n=11 H3K27M), including patients on an IRB-approved prospective observational study at Children's Hospital of Colorado for children and young adults with brain tumors undergoing patient-directed medical marijuana therapy (NCT03052738), and retrospective interviews with families of patients who underwent research autopsy at the University of Michigan. CBD was obtained through medical and recreational marijuana dispensaries without prescription; and given orally in all but one case (suppository) one to three times per day with a wide range of dosing (0.07 mg/kg to 25 mg/kg/day, Fig. 7A). No parents reported adverse effects from the

bioRxiv preprint doi: https://doi.org/10.1101/2021.05.10.443452; this version posted May 11, 2021. The copyright holder for this preprint (which was not certified by peer review) is the author/funder, who has granted bioRxiv a license to display the preprint in perpetuity. It is made available under aCC-BY-NC-ND 4.0 International license.

CBD aside from taste, and some reported improved nausea and anxiety control. We performed ID1 staining on autopsy samples from high-dose and low-dose H3K27M-mutant tumors. As representative cases, patient UMPED83, with the highest reported dosing (25 mg/kg/day CBD), demonstrated reduced ID1 staining on autopsy sample (Fig. 7B), while UMPED86 underwent low dosing (0.4 mg/kg/day) and demonstrated strong nuclear ID1 staining (Fig. 7C). Patients with pHGG undergoing CBD treatment showed variable ID1 staining in post-mortem tumor tissue, but lower average expression with higher-dose (>3 mg/kg/day) treatments (Fig. 7D).

Patients with H3K27M-mutant tumors treated with CBD (n=10) showed improved survival compared to historical controls (*20*), in both high (>3 mg/kg/day) and low (<3 mg/kg/day) CBD treatment groups (Fig. 7E, Supplemental Table 2). These data represent the promise and feasibility of CBD treatment in DIPG, with the clear need for further data in a prospective therapeutic clinical trial.

DISCUSSION

ID proteins are necessary for appropriate tissue differentiation during embryogenesis, and *ID1* is highly expressed in the normal developing brain followed by quiescence of *ID1* expression in CNS tissue postnatally (*40*). Consistent with the role of ID1 in the pathogenesis of multiple human diseases and cancers (*40-42*), our data indicate that ID1 promotes invasion in DIPG cells, which is a disease-defining feature of this infiltrative tumor. We propose a model by which ID1 is upregulated through multiple mechanisms (H3K27M, ACVR1, region/micro-environment) in order to “re-activate” prenatal brain developmental signaling. Our data support that *ID1*$^{+}$ AC-like DIPG tumor cells hijack the transcriptional program of developmental *ID1*$^{+}$ OAPC cells in the developing brain cells to produce a “migratory” transcriptional cell state (Fig.

bioRxiv preprint doi: https://doi.org/10.1101/2021.05.10.443452; this version posted May 11, 2021. The copyright holder for this preprint (which was not certified by peer review) is the author/funder, who has granted bioRxiv a license to display the preprint in perpetuity. It is made available under aCC-BY-NC-ND 4.0 International license.

8). We also demonstrate the ability to reverse this ID1-driven phenotype with CBD treatment, and the potential for optimization of this therapeutic targeting.

Our studies implicate an active epigenetic state at the *ID1* locus shared between H3K27M tumor cells and the prenatal precursor brain cells, which is consistent with prior studies focused on H3K27M mutations that have associated changes in H3K27ac/H3K27me3 with differential regulation of key DIPG-associated genes (*43, 44*). Additionally, we provide evidence that post-natal activation of ID1 in tumor cells replicates a prenatal "migratory" transcriptional state seen in a recently discovered subset of developing OAPC brain cells. These OAPCs (*Olig2*$^{+}$ *SPARCL1*$^{+}$*HOPX*$^{+}$ glial progenitor cells) were recently identified as astrocyte-like at the molecular and transcriptional levels (*28*). In line with this, we found AC-like DIPG cells to transcriptionally mimic the program of OAPCs, with the OAPC-marker *SPARCL1* and *ID1* co-localizing in a subset of H3K27M tumor cells. Interestingly, previous work has suggested a role for *SPARCL1* in promoting DIPG cell invasion into the subventricular zone (SVZ) (*45*). Secretion of SPARCL1 and pleiotrophin from neural precursor cells (NPCs) was shown to act as a chemoattractant for the DIPG cells, encouraging their infiltration into the SVZ (*45*). Our data demonstrate that *ID1* is most highly expressed by non-cycling AC-like cells in DIPG tumors and *SPARCL1* is one of the strongest expression markers of these cells. This raises the possibility that *SPARCL1* is expressed/secreted *within* DIPG cells, further coordinating or contributing to the invasion of DIPG tumor cells. While further studies are needed to confirm an ID1-driven OAPC/AC-like cellular state, our data raise important insights into the mechanisms underlying one of the most critical and problematic features of DIPG tumors: invasion.

Our data show that ID1 knockdown has the potential to severely impede DIPG tumor cell migration and invasion in pre-clinical models. These phenotypes are consistent with the inherent

bioRxiv preprint doi: https://doi.org/10.1101/2021.05.10.443452; this version posted May 11, 2021. The copyright holder for this preprint (which was not certified by peer review) is the author/funder, who has granted bioRxiv a license to display the preprint in perpetuity. It is made available under aCC-BY-NC-ND 4.0 International license.

invasion into normal brainstem tissue that is observed histologically in DIPGs, and with the role of ID1 in other cancers (*11, 42*). In our experiments involving both genetically-engineered and intracranial implantation models, H3K27M-mutant tumors cells with ID1 reduction show reduced tumor growth and invasion.

Cannabidiol is a non-toxic and non-psychoactive member of the endocannabinoid family found in *Cannabis sativa*. CBD has been observed to reduce *ID1* transcription in pre-clinical models of adult cancers (*12*). In the present study, CBD reduced DIPG cell viability and *ID1* expression at concentrations that are likely clinically achievable in the human brain. Our PK studies demonstrated peak brain concentrations of CBD above established IC_{50}, despite use of a human equivalent doses (*46*) of only 3 mg/kg, which is well below previously tolerated human CBD dosing. In a phase 1 study, adult patients showed excellent tolerance of oral CBD at 750 mg (15 mg/kg) daily with some non-dose limiting increases in diarrhea and somatic symptoms (muscle ache, fatigue) at 1500 mg (30 mg/kg) daily (*47*). This resulted in peak plasma concentrations of CBD of 1-5 uM (15 mg/kg) and 1.7-10 uM (30 mg/kg) depending on fat content in diet (*47*). Our data showed equivalent plasma and brain concentrations of CBD after IP administration. Previous work has shown that oral administration of CBD in mice results in a 3-4-fold higher concentration in the brain than plasma, likely due to the high lipophilicity of CBD (*35*). CBD is already being used for palliative purposes in pediatric oncology, and CBD has been shown to decrease *ID1* expression and associated oncogenic phenotypes in multiple other cancers in vivo (*11, 12, 48*). Mechanistically, our data suggest that CBD acts to regulate ID1 expression and DIPG cell proliferation partially through increasing intracellular levels of ROS, as previous studies have shown CBD to act through this mechanism in both breast cancer and GBM cells (*37, 38*).

bioRxiv preprint doi: https://doi.org/10.1101/2021.05.10.443452; this version posted May 11, 2021. The copyright holder for this preprint (which was not certified by peer review) is the author/funder, who has granted bioRxiv a license to display the preprint in perpetuity. It is made available under aCC-BY-NC-ND 4.0 International license.

Patients with H3K27M-mutant tumors treated with CBD off-trial show promising improvement in OS compared to historical controls. However, it is important to note that this is limited by the retrospective and heterogeneous nature of our cohort, as well as an unknown number of historical controls that may also have underwent treatment with CBD. Nevertheless, our data make significant strides in establishing the mechanism of this controversial and popular off-trial supplemental compound in high-risk brain tumor patients, and lays the groundwork for future clinical trials. A recent CBD formulation (Epidiolex) has been FDA-approved for epilepsy treatment (*49*), opening the door to a future clinical trial in DIPG (and other ID1-driven tumors).

Our data support a model in which multifactorial genetic and epigenetic processes promote ID1-driven prenatal development transcriptional programs, which also promote the invasive features of DIPG. These results improve our understanding of the pathogenesis of DIPG tumors and provide a strong argument for the inclusion of ID1-targeting therapies into future treatments.

METHODS

Study design

The objective of this work was to investigate the role of ID1 in the highly-invasive nature of DIPG and to determine the in vivo antitumor efficacy of genetic and pharmacologic inhibition of ID1 using our IUE *H3.3A*-K27M-mutated murine tumor model. We performed a comprehensive analysis of *ID1* expression by RNA-sequencing of DIPG tissue samples with $H3^{WT}$, H3K27M/$ACVR1^{WT}$, or H3K27M/$ACVR^{MUT}$. We next performed an integrative analysis of H3K27ac and H3K27me3 deposition at the *ID1* gene locus by performing Mint-ChIP-sequencing on these DIPG samples. We further performed transcriptional program analyses of

bioRxiv preprint doi: https://doi.org/10.1101/2021.05.10.443452; this version posted May 11, 2021. The copyright holder for this preprint (which was not certified by peer review) is the author/funder, who has granted bioRxiv a license to display the preprint in perpetuity. It is made available under aCC-BY-NC-ND 4.0 International license.

ID1-expressing DIPG tumor cells using publicly-available scRNA-seq datasets. To test the in vivo impact of ID1 inhibition, we performed *ID1* knockdown in our PPK tumor model. In vivo pharmacological inhibition of ID1 in our PPK tumor model was performed with CBD. Sample size and any data inclusion/exclusion were defined individually for each mouse experiment. The number of replicates varied between experiments and is presented in figure legends. We performed blinding for quantitative immunohistochemistry scoring of ID1 and Ki67 staining. Finally, we measured ID1 expression in DIPG patient samples which underwent different doses of CBD (non-prescribed) during the course of treatment (Supplement Table 2).

Murine IUE model of pHGG

All animal studies were conducted according to the guidelines approved by the University Committee on Use and Care of Animals (UCUCA) at the University of Michigan. IUE was performed using sterile technique on isoflurane/oxygen-anesthetized pregnant CD1 females at embryonic stage E13.5, using established methodology. In this study, we injected the following four plasmids together: [1] PBase, [2] PB-CAG-DNp53-Ires-Luciferase (dominant negative TP53 or TP53 hereafter), [3] PB-CAG-PdgfraD824V-Ires-eGFP (PDGFRA D842V), and [4] PB-CAG-H3.3 K27M-Ires-eGFP (H3K27M), referred to as “PPK” model (as previously published) (*17*) (see Supplementary for details).

Whole exome and transcriptome sequencing (Sick Kids, Toronto)

Use of patient tissues was approved by the Hospital for Sick Children (Toronto) Research Ethics Board. WES/WGS (accession EGAS00001000575) from DIPG samples plus matched normal was using DNA extracted from fresh-frozen tissues as described (*13*). Fresh-frozen tissue

bioRxiv preprint doi: https://doi.org/10.1101/2021.05.10.443452; this version posted May 11, 2021. The copyright holder for this preprint (which was not certified by peer review) is the author/funder, who has granted bioRxiv a license to display the preprint in perpetuity. It is made available under aCC-BY-NC-ND 4.0 International license.

was used for total RNA extraction with the RNeasy mini kit (QIAGEN, CA, USA) (see Supplementary for details).

Mint-ChIP-sequencing

Analyses for the two classical histone modifications H3K27ac and H3K27me3 representing accessible and repressed chromatin states were performed as part of a MiNT-ChIP analysis for 9 tumor samples of DIPG patients in comparison to a control tissue sample of healthy pons according to the protocol published by Buenstro et al., 2013 (see Supplementary for details).

ScRNA-seq analysis from developing brain and H3K27M-mutant DIPGs

Single-cell gene expression data and their clusters in the developing brain were obtained from GSE133531 (mouse pons), GSE120046 (human pons, gestational week 8-28), and GSE144462 (human cortex, gestational week 21-26) (see Supplementary for details).

Native ChIP-qPCR

Native ChIP-qPCR was performed on post-mortem tissue using antibodies against H3K27ac (2 μl, cat# 07360, Millipore Sigma), H3K27me3 (1 μg, cat# 07449, Millipore Sigma), and control IgG (2 μg Cat#12370, Millipore Sigma) (see Supplementary for details).

Invasion assay

Invasion assays were performed using growth factor-reduced Matrigel invasion chambers (Cat #354483, Corning) as previously described (see Supplementary for details) (*50*).

bioRxiv preprint doi: https://doi.org/10.1101/2021.05.10.443452; this version posted May 11, 2021. The copyright holder for this preprint (which was not certified by peer review) is the author/funder, who has granted bioRxiv a license to display the preprint in perpetuity. It is made available under aCC-BY-NC-ND 4.0 International license.

Migration (scratch) assay

Scratches were made in 80%-confluent 6-well plates, and migration was monitored using the IncuCyte® system (see Supplementary for details).

CBD treatment studies in murine IUE PPK model

Mice harboring IUE-generated PPK HGG tumors were treated with CBD when tumors reached logarithmic growth phase (minimum 2 x 10^6 photons/sec via bioluminescent imaging). Mice litters from each experimental group were randomized to treatment with: (A) 15 mg/kg CBD (10% CBD suspended in Ethanol, 80% DPBS, 10% Tween-80) and (B) control treatment (10% Ethanol, 80% DPBS, 10% Tween-80). Mice were treated 5 days/week until morbidity (see Supplementary for details).

CBD pharmacokinetic analysis

CBD administration to non-tumor bearing CD1 mice and PPK tumor bearing mice for PK studies were performed by IP injection at zero time point. Timeline for CBD injection and plasma, brainstem and/or tumor collection were depicted in Fig. 7 E-F (see Supplementary for details).

Human studies

Informed consent was obtained for all patient samples. Two patients (CHC001 and CHC002) were enrolled on an ongoing IRB-approved prospective observational study at

bioRxiv preprint doi: https://doi.org/10.1101/2021.05.10.443452; this version posted May 11, 2021. The copyright holder for this preprint (which was not certified by peer review) is the author/funder, who has granted bioRxiv a license to display the preprint in perpetuity. It is made available under aCC-BY-NC-ND 4.0 International license.

Children's Hospital of Colorado for children and young adults with brain tumors undergoing patient-directed medical marijuana therapy (NCT03052738) (see Supplementary for details).

Supplementary Materials

Materials and Methods

Fig. S1. *ID1* expression in DIPG by cell malignancy and tumor location.

Fig. S2. Multifocal ChIP-qPCR analysis of *ID1* expression in human DIPG.

Fig. S3. *ID1* expression from scRNA-seq of six different H3K27M-DMG patients across varying regions and malignant cell types.

Fig. S4. In situ hybridization for *ID1* RNA in developing mouse brain.

Fig. S5. H3K27ac at *ID1* locus during murine development.

Fig. S6. *ID1* expression in varying cell types during normal murine pontine development.

Fig. S7. *ID1* expression from single-cell transcriptome analysis of varying cell types in normal developing murine pons.

Fig. S8. *ID1* expression from scRNA-seq of four different H3K27M-DMG patients across varying malignant cell types.

Fig. S9. Gene ontology (GO) analysis of higher *ID1*-expressing AC-like cells from H3K27M-mutated tumor patients.

Fig. S10. *ID1* knockdown in HEK293 cells.

Fig. S11. Impact of CBD treatment on ID1 expression in human DIPG cells.

bioRxiv preprint doi: https://doi.org/10.1101/2021.05.10.443452; this version posted May 11, 2021. The copyright holder for this preprint (which was not certified by peer review) is the author/funder, who has granted bioRxiv a license to display the preprint in perpetuity. It is made available under aCC-BY-NC-ND 4.0 International license.

Fig. S12. Effect of pharmacologic (CBD) suppression of ID1 on DIPG007 and PBT-29 tumor cell invasion and migration.

Fig. S13. ID1-deficient DIPG007 cells display slower in vivo tumor growth.

Fig. S14. Tumor cell invasion assessment in CBD- vs control-treated PPK mice.

Fig. S15. Detailed vector map of pGIPZ lentiviral vector.

Table S1. Primer sequences for use in ChIP-qPCR and qPCR.

Table S2. Clinical details of pHGG patients treated with CBD.

References and Notes

1. K. M. Schroeder, C. M. Hoeman, O. J. Becher, Children are not just little adults: recent advances in understanding of diffuse intrinsic pontine glioma biology. *Pediatr Res* **75**, 205-209 (2014).

2. Z. Miklja, A. Pasternak, S. Stallard, T. Nicolaides, C. Kline-Nunnally, B. Cole, R. Beroukhim, P. Bandopadhayay, S. Chi, S. H. Ramkissoon, B. Mullan, A. K. Bruzek, A. Gauthier, T. Garcia, C. Atchison, B. Marini, M. Fouladi, D. W. Parsons, S. Leary, S. Mueller, K. L. Ligon, C. Koschmann, Molecular profiling and targeted therapy in pediatric gliomas: review and consensus recommendations. *Neuro Oncol*, (2019).

3. D. Castel, C. Philippe, R. Calmon, L. Le Dret, N. Truffaux, N. Boddaert, M. Pages, K. R. Taylor, P. Saulnier, L. Lacroix, A. Mackay, C. Jones, C. Sainte-Rose, T. Blauwblomme, F. Andreiuolo, S. Puget, J. Grill, P. Varlet, M. A. Debily, Histone H3F3A and

bioRxiv preprint doi: https://doi.org/10.1101/2021.05.10.443452; this version posted May 11, 2021. The copyright holder for this preprint (which was not certified by peer review) is the author/funder, who has granted bioRxiv a license to display the preprint in perpetuity. It is made available under aCC-BY-NC-ND 4.0 International license.

HIST1H3B K27M mutations define two subgroups of diffuse intrinsic pontine gliomas with different prognosis and phenotypes. *Acta Neuropathol* **130**, 815-827 (2015).

4. D. A. Khuong-Quang, P. Buczkowicz, P. Rakopoulos, X. Y. Liu, A. M. Fontebasso, E. Bouffet, U. Bartels, S. Albrecht, J. Schwartzentruber, L. Letourneau, M. Bourgey, G. Bourque, A. Montpetit, G. Bourret, P. Lepage, A. Fleming, P. Lichter, M. Kool, A. von Deimling, D. Sturm, A. Korshunov, D. Faury, D. T. Jones, J. Majewski, S. M. Pfister, N. Jabado, C. Hawkins, K27M mutation in histone H3.3 defines clinically and biologically distinct subgroups of pediatric diffuse intrinsic pontine gliomas. *Acta Neuropathol* **124**, 439-447 (2012).

5. K. M. Chan, D. Fang, H. Gan, R. Hashizume, C. Yu, M. Schroeder, N. Gupta, S. Mueller, C. D. James, R. Jenkins, J. Sarkaria, Z. Zhang, The histone H3.3K27M mutation in pediatric glioma reprograms H3K27 methylation and gene expression. *Genes Dev* **27**, 985-990 (2013).

6. F. Mohammad, S. Weissmann, B. Leblanc, D. P. Pandey, J. W. Hojfeldt, I. Comet, C. Zheng, J. V. Johansen, N. Rapin, B. T. Porse, A. Tvardovskiy, O. N. Jensen, N. G. Olaciregui, C. Lavarino, M. Sunol, C. de Torres, J. Mora, A. M. Carcaboso, K. Helin, EZH2 is a potential therapeutic target for H3K27M-mutant pediatric gliomas. *Nat Med* **23**, 483-492 (2017).

7. S. Nagaraja, M. A. Quezada, S. M. Gillespie, M. Arzt, J. J. Lennon, P. J. Woo, V. Hovestadt, M. Kambhampati, M. G. Filbin, M. L. Suva, J. Nazarian, M. Monje, Histone Variant and Cell Context Determine H3K27M Reprogramming of the Enhancer Landscape and Oncogenic State. *Mol Cell* **76**, 965-980 e912 (2019).

bioRxiv preprint doi: https://doi.org/10.1101/2021.05.10.443452; this version posted May 11, 2021. The copyright holder for this preprint (which was not certified by peer review) is the author/funder, who has granted bioRxiv a license to display the preprint in perpetuity. It is made available under aCC-BY-NC-ND 4.0 International license.

8. J. D. Norton, R. W. Deed, G. Craggs, F. Sablitzky, Id helix-loop-helix proteins in cell growth and differentiation. *Trends Cell Biol* **8**, 58-65 (1998).

9. R. Benezra, R. L. Davis, D. Lockshon, D. L. Turner, H. Weintraub, The protein Id: a negative regulator of helix-loop-helix DNA binding proteins. *Cell* **61**, 49-59 (1990).

10. S. Fong, R. J. Debs, P. Y. Desprez, Id genes and proteins as promising targets in cancer therapy. *Trends Mol Med* **10**, 387-392 (2004).

11. L. Soroceanu, R. Murase, C. Limbad, E. Singer, J. Allison, I. Adrados, R. Kawamura, A. Pakdel, Y. Fukuyo, D. Nguyen, S. Khan, R. Arauz, G. L. Yount, D. H. Moore, P. Y. Desprez, S. D. McAllister, Id-1 is a key transcriptional regulator of glioblastoma aggressiveness and a novel therapeutic target. *Cancer Res* **73**, 1559-1569 (2013).

12. S. D. McAllister, R. T. Christian, M. P. Horowitz, A. Garcia, P. Y. Desprez, Cannabidiol as a novel inhibitor of Id-1 gene expression in aggressive breast cancer cells. *Mol Cancer Ther* **6**, 2921-2927 (2007).

13. P. Buczkowicz, C. Hoeman, P. Rakopoulos, S. Pajovic, L. Letourneau, M. Dzamba, A. Morrison, P. Lewis, E. Bouffet, U. Bartels, J. Zuccaro, S. Agnihotri, S. Ryall, M. Barszczyk, Y. Chornenkyy, M. Bourgey, G. Bourque, A. Montpetit, F. Cordero, P. Castelo-Branco, J. Mangerel, U. Tabori, K. C. Ho, A. Huang, K. R. Taylor, A. Mackay, A. E. Bendel, J. Nazarian, J. R. Fangusaro, M. A. Karajannis, D. Zagzag, N. K. Foreman, A. Donson, J. V. Hegert, A. Smith, J. Chan, L. Lafay-Cousin, S. Dunn, J. Hukin, C. Dunham, K. Scheinemann, J. Michaud, S. Zelcer, D. Ramsay, J. Cain, C. Brennan, M. M. Souweidane, C. Jones, C. D. Allis, M. Brudno, O. Becher, C. Hawkins, Genomic analysis of diffuse intrinsic pontine gliomas identifies three molecular subgroups and recurrent activating ACVR1 mutations. *Nature genetics* **46**, 451-456 (2014).

bioRxiv preprint doi: https://doi.org/10.1101/2021.05.10.443452; this version posted May 11, 2021. The copyright holder for this preprint (which was not certified by peer review) is the author/funder, who has granted bioRxiv a license to display the preprint in perpetuity. It is made available under aCC-BY-NC-ND 4.0 International license.

14. C. M. Hoeman, F. J. Cordero, G. Hu, K. Misuraca, M. M. Romero, H. J. Cardona, J. Nazarian, R. Hashizume, R. McLendon, P. Yu, D. Procissi, S. Gadd, O. J. Becher, ACVR1 R206H cooperates with H3.1K27M in promoting diffuse intrinsic pontine glioma pathogenesis. *Nat Commun* **10**, 1023 (2019).

15. J. Fortin, R. Tian, I. Zarrabi, G. Hill, E. Williams, G. Sanchez-Duffhues, M. Thorikay, P. Ramachandran, R. Siddaway, J. F. Wong, A. Wu, L. N. Apuzzo, J. Haight, A. You-Ten, B. E. Snow, A. Wakeham, D. J. Goldhamer, D. Schramek, A. N. Bullock, P. T. Dijke, C. Hawkins, T. W. Mak, Mutant ACVR1 Arrests Glial Cell Differentiation to Drive Tumorigenesis in Pediatric Gliomas. *Cancer Cell* **37**, 308-323 e312 (2020).

16. B. Schmierer, C. S. Hill, TGFβ–SMAD signal transduction: molecular specificity and functional flexibility. *Nature reviews Molecular cell biology* **8**, 970-982 (2007).

17. Z. Miklja, V. N. Yadav, R. T. Cartaxo, R. Siada, C. C. Thomas, J. R. Cummings, B. Mullan, S. Stallard, A. Paul, A. K. Bruzek, Everolimus improves the efficacy of dasatinib in PDGFRα-driven glioma. *The Journal of clinical investigation* **130**, (2020).

18. P. W. Lewis, M. M. Muller, M. S. Koletsky, F. Cordero, S. Lin, L. A. Banaszynski, B. A. Garcia, T. W. Muir, O. J. Becher, C. D. Allis, Inhibition of PRC2 activity by a gain-of-function H3 mutation found in pediatric glioblastoma. *Science* **340**, 857-861 (2013).

19. M. G. Filbin, I. Tirosh, V. Hovestadt, M. L. Shaw, L. E. Escalante, N. D. Mathewson, C. Neftel, N. Frank, K. Pelton, C. M. Hebert, C. Haberler, K. Yizhak, J. Gojo, K. Egervari, C. Mount, P. van Galen, D. M. Bonal, Q. D. Nguyen, A. Beck, C. Sinai, T. Czech, C. Dorfer, L. Goumnerova, C. Lavarino, A. M. Carcaboso, J. Mora, R. Mylvaganam, C. C. Luo, A. Peyrl, M. Popovic, A. Azizi, T. T. Batchelor, M. P. Frosch, M. Martinez-Lage, M. W. Kieran, P. Bandopadhayay, R. Beroukhim, G. Fritsch, G. Getz, O. Rozenblatt-

bioRxiv preprint doi: https://doi.org/10.1101/2021.05.10.443452; this version posted May 11, 2021. The copyright holder for this preprint (which was not certified by peer review) is the author/funder, who has granted bioRxiv a license to display the preprint in perpetuity. It is made available under aCC-BY-NC-ND 4.0 International license.

Rosen, K. W. Wucherpfennig, D. N. Louis, M. Monje, I. Slavc, K. L. Ligon, T. R. Golub, A. Regev, B. E. Bernstein, M. L. Suva, Developmental and oncogenic programs in H3K27M gliomas dissected by single-cell RNA-seq. *Science* **360**, 331-335 (2018).

20. A. Mackay, A. Burford, D. Carvalho, E. Izquierdo, J. Fazal-Salom, K. R. Taylor, L. Bjerke, M. Clarke, M. Vinci, M. Nandhabalan, S. Temelso, S. Popov, V. Molinari, P. Raman, A. J. Waanders, H. J. Han, S. Gupta, L. Marshall, S. Zacharoulis, S. Vaidya, H. C. Mandeville, L. R. Bridges, A. J. Martin, S. Al-Sarraj, C. Chandler, H. K. Ng, X. Li, K. Mu, S. Trabelsi, D. H. Brahim, A. N. Kisljakov, D. M. Konovalov, A. S. Moore, A. M. Carcaboso, M. Sunol, C. de Torres, O. Cruz, J. Mora, L. I. Shats, J. N. Stavale, L. T. Bidinotto, R. M. Reis, N. Entz-Werle, M. Farrell, J. Cryan, D. Crimmins, J. Caird, J. Pears, M. Monje, M. A. Debily, D. Castel, J. Grill, C. Hawkins, H. Nikbakht, N. Jabado, S. J. Baker, S. M. Pfister, D. T. W. Jones, M. Fouladi, A. O. von Bueren, M. Baudis, A. Resnick, C. Jones, Integrated Molecular Meta-Analysis of 1,000 Pediatric High-Grade and Diffuse Intrinsic Pontine Glioma. *Cancer Cell* **32**, 520-537 e525 (2017).

21. S. F. Schoppmann, M. Schindl, G. Bayer, K. Aumayr, J. Dienes, R. Horvat, M. Rudas, M. Gnant, R. Jakesz, P. Birner, Overexpression of Id-1 is associated with poor clinical outcome in node negative breast cancer. *Int J Cancer* **104**, 677-682 (2003).

22. G. Wu, A. K. Diaz, B. S. Paugh, S. L. Rankin, B. Ju, Y. Li, X. Zhu, C. Qu, X. Chen, J. Zhang, J. Easton, M. Edmonson, X. Ma, C. Lu, P. Nagahawatte, E. Hedlund, M. Rusch, S. Pounds, T. Lin, A. Onar-Thomas, R. Huether, R. Kriwacki, M. Parker, P. Gupta, J. Becksfort, L. Wei, H. L. Mulder, K. Boggs, B. Vadodaria, D. Yergeau, J. C. Russell, K. Ochoa, R. S. Fulton, L. L. Fulton, C. Jones, F. A. Boop, A. Broniscer, C. Wetmore, A. Gajjar, L. Ding, E. R. Mardis, R. K. Wilson, M. R. Taylor, J. R. Downing, D. W. Ellison,

bioRxiv preprint doi: https://doi.org/10.1101/2021.05.10.443452; this version posted May 11, 2021. The copyright holder for this preprint (which was not certified by peer review) is the author/funder, who has granted bioRxiv a license to display the preprint in perpetuity. It is made available under aCC-BY-NC-ND 4.0 International license.

J. Zhang, S. J. Baker, The genomic landscape of diffuse intrinsic pontine glioma and pediatric non-brainstem high-grade glioma. *Nat Genet* **46**, 444-450 (2014).

23. E. P. Consortium, An integrated encyclopedia of DNA elements in the human genome. *Nature* **489**, 57-74 (2012).

24. C. A. Davis, B. C. Hitz, C. A. Sloan, E. T. Chan, J. M. Davidson, I. Gabdank, J. A. Hilton, K. Jain, U. K. Baymuradov, A. K. Narayanan, K. C. Onate, K. Graham, S. R. Miyasato, T. R. Dreszer, J. S. Strattan, O. Jolanki, F. Y. Tanaka, J. M. Cherry, The Encyclopedia of DNA elements (ENCODE): data portal update. *Nucleic Acids Res* **46**, D794-D801 (2018).

25. X. Fan, Y. Fu, X. Zhou, L. Sun, M. Yang, M. Wang, R. Chen, Q. Wu, J. Yong, J. Dong, L. Wen, J. Qiao, X. Wang, F. Tang, Single-cell transcriptome analysis reveals cell lineage specification in temporal-spatial patterns in human cortical development. *Sci Adv* **6**, eaaz2978 (2020).

26. S. Jessa, A. Blanchet-Cohen, B. Krug, M. Vladoiu, M. Coutelier, D. Faury, B. Poreau, N. De Jay, S. Hebert, J. Monlong, W. T. Farmer, L. K. Donovan, Y. Hu, M. K. McConechy, F. M. G. Cavalli, L. G. Mikael, B. Ellezam, M. Richer, A. Allaire, A. G. Weil, J. Atkinson, J. P. Farmer, R. W. R. Dudley, V. Larouche, L. Crevier, S. Albrecht, M. G. Filbin, H. Sartelet, P. E. Lutz, C. Nagy, G. Turecki, S. Costantino, P. B. Dirks, K. K. Murai, G. Bourque, J. Ragoussis, L. Garzia, M. D. Taylor, N. Jabado, C. L. Kleinman, Stalled developmental programs at the root of pediatric brain tumors. *Nature genetics* **51**, 1702-1713 (2019).

bioRxiv preprint doi: https://doi.org/10.1101/2021.05.10.443452; this version posted May 11, 2021. The copyright holder for this preprint (which was not certified by peer review) is the author/funder, who has granted bioRxiv a license to display the preprint in perpetuity. It is made available under aCC-BY-NC-ND 4.0 International license.

27. D. Lyden, A. Z. Young, D. Zagzag, W. Yan, W. Gerald, R. O'Reilly, B. L. Bader, R. O. Hynes, Y. Zhuang, K. Manova, R. Benezra, Id1 and Id3 are required for neurogenesis, angiogenesis and vascularization of tumour xenografts. *Nature* **401**, 670-677 (1999).

28. Y. Fu, M. Yang, H. Yu, Y. Wang, X. Wu, J. Yong, Y. Mao, Y. Cui, X. Fan, L. Wen, J. Qiao, F. Tang, Heterogeneity of glial progenitor cells during the neurogenesis-to-gliogenesis switch in the developing human cerebral cortex. *Cell Rep* **34**, 108788 (2021).

29. R. Sachdeva, M. Wu, S. Smiljanic, O. Kaskun, K. Ghannad-Zadeh, A. Celebre, K. Isaev, A. S. Morrissy, J. Guan, J. Tong, J. Chan, T. M. Wilson, S. Al-Omaishi, D. G. Munoz, P. B. Dirks, M. F. Moran, M. D. Taylor, J. Reimand, S. Das, ID1 Is Critical for Tumorigenesis and Regulates Chemoresistance in Glioblastoma. *Cancer Res* **79**, 4057-4071 (2019).

30. K. Tada, K. Kawahara, S. Matsushita, T. Hashiguchi, I. Maruyama, T. Kanekura, MK615, a Prunus mume Steb. Et Zucc ('Ume') extract, attenuates the growth of A375 melanoma cells by inhibiting the ERK1/2-Id-1 pathway. *Phytother Res* **26**, 833-838 (2012).

31. J. I. Huh, A. Calvo, R. Charles, J. E. Green, Distinct tumor stage-specific inhibitory effects of 2-methoxyestradiol in a breast cancer mouse model associated with Id-1 expression. *Cancer Res* **66**, 3495-3503 (2006).

32. F. Afrin, M. Chi, A. L. Eamens, R. J. Duchatel, A. M. Douglas, J. Schneider, C. Gedye, A. S. Woldu, M. D. Dun, Can Hemp Help? Low-THC Cannabis and Non-THC Cannabinoids for the Treatment of Cancer. *Cancers (Basel)* **12**, (2020).

33. G. Wilkie, B. Sakr, T. Rizack, Medical Marijuana Use in Oncology: A Review. *JAMA Oncol* **2**, 670-675 (2016).

bioRxiv preprint doi: https://doi.org/10.1101/2021.05.10.443452; this version posted May 11, 2021. The copyright holder for this preprint (which was not certified by peer review) is the author/funder, who has granted bioRxiv a license to display the preprint in perpetuity. It is made available under aCC-BY-NC-ND 4.0 International license.

34. M. M. Bergamaschi, R. H. Queiroz, A. W. Zuardi, J. A. Crippa, Safety and side effects of cannabidiol, a Cannabis sativa constituent. *Curr Drug Saf* **6**, 237-249 (2011).

35. S. Deiana, A. Watanabe, Y. Yamasaki, N. Amada, M. Arthur, S. Fleming, H. Woodcock, P. Dorward, B. Pigliacampo, S. Close, B. Platt, G. Riedel, Plasma and brain pharmacokinetic profile of cannabidiol (CBD), cannabidivarine (CBDV), Delta(9)-tetrahydrocannabivarin (THCV) and cannabigerol (CBG) in rats and mice following oral and intraperitoneal administration and CBD action on obsessive-compulsive behaviour. *Psychopharmacology (Berl)* **219**, 859-873 (2012).

36. O. Kovalchuk, I. Kovalchuk, Cannabinoids as anticancer therapeutic agents. *Cell Cycle* **19**, 961-989 (2020).

37. S. D. McAllister, R. Murase, R. T. Christian, D. Lau, A. J. Zielinski, J. Allison, C. Almanza, A. Pakdel, J. Lee, C. Limbad, Y. Liu, R. J. Debs, D. H. Moore, P. Y. Desprez, Pathways mediating the effects of cannabidiol on the reduction of breast cancer cell proliferation, invasion, and metastasis. *Breast Cancer Res Treat* **129**, 37-47 (2011).

38. E. Singer, J. Judkins, N. Salomonis, L. Matlaf, P. Soteropoulos, S. McAllister, L. Soroceanu, Reactive oxygen species-mediated therapeutic response and resistance in glioblastoma. *Cell Death Dis* **6**, e1601 (2015).

39. G. Wilkie, B. Sakr, T. Rizack, Medical marijuana use in oncology: a review. *JAMA oncology* **2**, 670-675 (2016).

40. S. F. Tzeng, J. de Vellis, Id1, Id2, and Id3 gene expression in neural cells during development. *Glia* **24**, 372-381 (1998).

41. M. T. Ling, X. Wang, X. Zhang, Y. C. Wong, The multiple roles of Id-1 in cancer progression. *Differentiation* **74**, 481-487 (2006).

bioRxiv preprint doi: https://doi.org/10.1101/2021.05.10.443452; this version posted May 11, 2021. The copyright holder for this preprint (which was not certified by peer review) is the author/funder, who has granted bioRxiv a license to display the preprint in perpetuity. It is made available under aCC-BY-NC-ND 4.0 International license.

42. R. Sachdeva, M. Wu, S. Smiljanic, O. Kaskun, K. Ghannad-Zadeh, A. Celebre, K. Isaev, A. S. Morrissy, J. Guan, J. Tong, J. Chan, T. M. Wilson, S. Al-Omaishi, D. G. Munoz, P. B. Dirks, M. F. Moran, M. D. Taylor, J. Reimand, S. Das, ID1 Is Critical for Tumorigenesis and Regulates Chemoresistance in Glioblastoma. *Cancer Res*, (2019).

43. A. Piunti, R. Hashizume, M. A. Morgan, E. T. Bartom, C. M. Horbinski, S. A. Marshall, E. J. Rendleman, Q. Ma, Y. H. Takahashi, A. R. Woodfin, A. V. Misharin, N. A. Abshiru, R. R. Lulla, A. M. Saratsis, N. L. Kelleher, C. D. James, A. Shilatifard, Therapeutic targeting of polycomb and BET bromodomain proteins in diffuse intrinsic pontine gliomas. *Nat Med* **23**, 493-500 (2017).

44. J. D. Larson, L. H. Kasper, B. S. Paugh, H. Jin, G. Wu, C. H. Kwon, Y. Fan, T. I. Shaw, A. B. Silveira, C. Qu, R. Xu, X. Zhu, J. Zhang, H. R. Russell, J. L. Peters, D. Finkelstein, B. Xu, T. Lin, C. L. Tinkle, Z. Patay, A. Onar-Thomas, S. B. Pounds, P. J. McKinnon, D. W. Ellison, J. Zhang, S. J. Baker, Histone H3.3 K27M Accelerates Spontaneous Brainstem Glioma and Drives Restricted Changes in Bivalent Gene Expression. *Cancer Cell* **35**, 140-155 e147 (2019).

45. E. Y. Qin, D. D. Cooper, K. L. Abbott, J. Lennon, S. Nagaraja, A. Mackay, C. Jones, H. Vogel, P. K. Jackson, M. Monje, Neural Precursor-Derived Pleiotrophin Mediates Subventricular Zone Invasion by Glioma. *Cell* **170**, 845-859 e819 (2017).

46. S. Reagan-Shaw, M. Nihal, N. Ahmad, Dose translation from animal to human studies revisited. *The FASEB journal* **22**, 659-661 (2008).

47. L. Taylor, B. Gidal, G. Blakey, B. Tayo, G. Morrison, A phase I, randomized, double-blind, placebo-controlled, single ascending dose, multiple dose, and food effect trial of

bioRxiv preprint doi: https://doi.org/10.1101/2021.05.10.443452; this version posted May 11, 2021. The copyright holder for this preprint (which was not certified by peer review) is the author/funder, who has granted bioRxiv a license to display the preprint in perpetuity. It is made available under aCC-BY-NC-ND 4.0 International license.

the safety, tolerability and pharmacokinetics of highly purified cannabidiol in healthy subjects. *CNS drugs* **32**, 1053-1067 (2018).

48. C. T. Campbell, M. S. Phillips, K. Manasco, Cannabinoids in Pediatrics. *J Pediatr Pharmacol Ther* **22**, 176-185 (2017).

49. O. Devinsky, C. Verducci, E. A. Thiele, L. C. Laux, A. D. Patel, F. Filloux, J. P. Szaflarski, A. Wilfong, G. D. Clark, Y. D. Park, L. E. Seltzer, E. M. Bebin, R. Flamini, R. T. Wechsler, D. Friedman, Open-label use of highly purified CBD (Epidiolex(R)) in patients with CDKL5 deficiency disorder and Aicardi, Dup15q, and Doose syndromes. *Epilepsy Behav* **86**, 131-137 (2018).

50. C. R. Justus, N. Leffler, M. Ruiz-Echevarria, L. V. Yang, In vitro cell migration and invasion assays. *J Vis Exp*, (2014).

51. S. Pajovic, R. Siddaway, T. Bridge, J. Sheth, P. Rakopoulos, B. Kim, S. Ryall, S. Agnihotri, L. Phillips, M. Yu, C. Li, S. Milos, P. Patel, D. Srikanthan, A. Huang, C. Hawkins, Epigenetic activation of a RAS/MYC axis in H3.3K27M-driven cancer. *Nat Commun* **11**, 6216 (2020).

52. A. M. Bolger, M. Lohse, B. Usadel, Trimmomatic: a flexible trimmer for Illumina sequence data. *Bioinformatics* **30**, 2114-2120 (2014).

53. B. Li, C. N. Dewey, RSEM: accurate transcript quantification from RNA-Seq data with or without a reference genome. *BMC Bioinformatics* **12**, 323 (2011).

54. D. Pratt, S. Camelo-Piragua, K. McFadden, D. Leung, R. Mody, A. Chinnaiyan, C. Koschmann, S. Venneti, in *Acta neuropathologica communications*. (England, 2018), vol. 6, pp. 24.

bioRxiv preprint doi: https://doi.org/10.1101/2021.05.10.443452; this version posted May 11, 2021. The copyright holder for this preprint (which was not certified by peer review) is the author/funder, who has granted bioRxiv a license to display the preprint in perpetuity. It is made available under aCC-BY-NC-ND 4.0 International license.

55. C. Koschmann, Y.-M. Wu, C. Kumar-Sinha, R. Lonigro, P. Vats, K. Kasaian, M. Cieslik, X. Cao, B. Anderson, K. Frank, Clinically integrated sequencing alters therapy in children and young adults with high-risk glial brain tumors. *JCO precision oncology* **2**, 1-34 (2018).

56. H. C. Gits, M. Anderson, S. Stallard, D. Pratt, B. Zon, C. Howell, C. Kumar-Sinha, P. Vats, K. Kasaian, D. Polan, M. Matuszak, D. E. Spratt, M. Leonard, T. Qin, L. Zhao, J. Leach, B. Chaney, N. Y. Escorza, J. Hendershot, B. Jones, C. Fuller, S. Leary, U. Bartels, E. Bouffet, T. I. Yock, P. Robertson, R. Mody, S. Venneti, A. M. Chinnaiyan, M. Fouladi, N. G. Gottardo, C. Koschmann, Medulloblastoma therapy generates risk of a poorly-prognostic H3 wild-type subgroup of diffuse intrinsic pontine glioma: a report from the International DIPG Registry. *Acta neuropathologica communications* **6**, 67 (2018).

57. S. K. Patel, R. M. Hartley, X. Wei, R. Furnish, F. Escobar-Riquelme, H. Bear, K. Choi, C. Fuller, T. N. Phoenix, Generation of diffuse intrinsic pontine glioma mouse models by brainstem-targeted in utero electroporation. *Neuro-oncology* **22**, 381-392 (2020).

58. L. J. Donovan LL, Native Chromatin Immunoprecipitation from Brain Tissue Using Magnetic Beads. *Medicinal Chemistry* **4**, 3 (2014).

59. S. Bender, Y. Tang, A. M. Lindroth, V. Hovestadt, D. T. Jones, M. Kool, M. Zapatka, P. A. Northcott, D. Sturm, W. Wang, B. Radlwimmer, J. W. Hojfeldt, N. Truffaux, D. Castel, S. Schubert, M. Ryzhova, H. Seker-Cin, J. Gronych, P. D. Johann, S. Stark, J. Meyer, T. Milde, M. Schuhmann, M. Ebinger, C. M. Monoranu, A. Ponnuswami, S. Chen, C. Jones, O. Witt, V. P. Collins, A. von Deimling, N. Jabado, S. Puget, J. Grill, K. Helin, A. Korshunov, P. Lichter, M. Monje, C. Plass, Y. J. Cho, S. M. Pfister, Reduced

bioRxiv preprint doi: https://doi.org/10.1101/2021.05.10.443452; this version posted May 11, 2021. The copyright holder for this preprint (which was not certified by peer review) is the author/funder, who has granted bioRxiv a license to display the preprint in perpetuity. It is made available under aCC-BY-NC-ND 4.0 International license.

H3K27me3 and DNA hypomethylation are major drivers of gene expression in K27M mutant pediatric high-grade gliomas. *Cancer Cell* **24**, 660-672 (2013).

60. T. D. Schmittgen, K. J. Livak, Analyzing real-time PCR data by the comparative C(T) method. *Nat Protoc* **3**, 1101-1108 (2008).

61. M. Lerdrup, J. V. Johansen, S. Agrawal-Singh, K. Hansen, An interactive environment for agile analysis and visualization of ChIP-sequencing data. *Nat Struct Mol Biol* **23**, 349-357 (2016).

62. J. T. Robinson, H. Thorvaldsdottir, W. Winckler, M. Guttman, E. S. Lander, G. Getz, J. P. Mesirov, Integrative genomics viewer. *Nat Biotechnol* **29**, 24-26 (2011).

63. M. V. Kuleshov, M. R. Jones, A. D. Rouillard, N. F. Fernandez, Q. Duan, Z. Wang, S. Koplev, S. L. Jenkins, K. M. Jagodnik, A. Lachmann, M. G. McDermott, C. D. Monteiro, G. W. Gundersen, A. Ma'ayan, Enrichr: a comprehensive gene set enrichment analysis web server 2016 update. *Nucleic Acids Res* **44**, W90-97 (2016).

64. C. C. Liang, A. Y. Park, J. L. Guan, In vitro scratch assay: a convenient and inexpensive method for analysis of cell migration in vitro. *Nat Protoc* **2**, 329-333 (2007).

Acknowledgments: The authors thank the patients and their families for participation in this study.

Funding:
National Institutes of Health/National Institute of Neurological Disorders and Stroke grant K08-NS099427-01 (CK)
The University of Michigan Chad Carr Pediatric Brain Tumor Center
The ChadTough Defeat DIPG Foundation
The DIPG Collaborative
U CAN-CER VIVE
Catching Up with Jack
The Morgan Behen Golf Classic

bioRxiv preprint doi: https://doi.org/10.1101/2021.05.10.443452; this version posted May 11, 2021. The copyright holder for this preprint (which was not certified by peer review) is the author/funder, who has granted bioRxiv a license to display the preprint in perpetuity. It is made available under aCC-BY-NC-ND 4.0 International license.

National Institutes of Health Clinical Sequencing Exploratory Research Award grant 1UM1HG006508 (AC)
National Institutes of Health grant R44CA206723 (SM and PYD)
The Research Council of Norway 187615 (SMW)
The South-Eastern Norway Regional Health Authority (SMW)
The University of Oslo (SMW)

Author contributions:
Conception and design of study: VNY, MKH, CK
Acquisition, analysis, or interpretation of data: VNY, MKH, DM, CT, JRC, TY, RW, RoS, MB, SS, TQ, BM, RuS, RR, MN, KFG, MAHG, KD, NAV, JL, MGF, XC, MGC, PRL, RM, AC, PYD, SM, CH, SMW, SV, CK
Drafting and revising the written manuscript: VNY, MKH, JRC, RuS, CK
Final approval of version to be published: VNY, MKH, DM, CT, JRC, TY, RW, RoS, MB, SS, TQ, BM, RuS, RR, MN, KFG, MAHG, KD, NAV, SVS, JS, JL, MGF, XC, MGC, PRL, RM, AC, PYD, SM, CH, SMW, SV, CK

Competing interests: Authors declare that they have no competing interests.

Data and materials availability: All data are available in the main text or the supplementary materials.

bioRxiv preprint doi: https://doi.org/10.1101/2021.05.10.443452; this version posted May 11, 2021. The copyright holder for this preprint (which was not certified by peer review) is the author/funder, who has granted bioRxiv a license to display the preprint in perpetuity. It is made available under aCC-BY-NC-ND 4.0 International license.

Figures

Figure 1

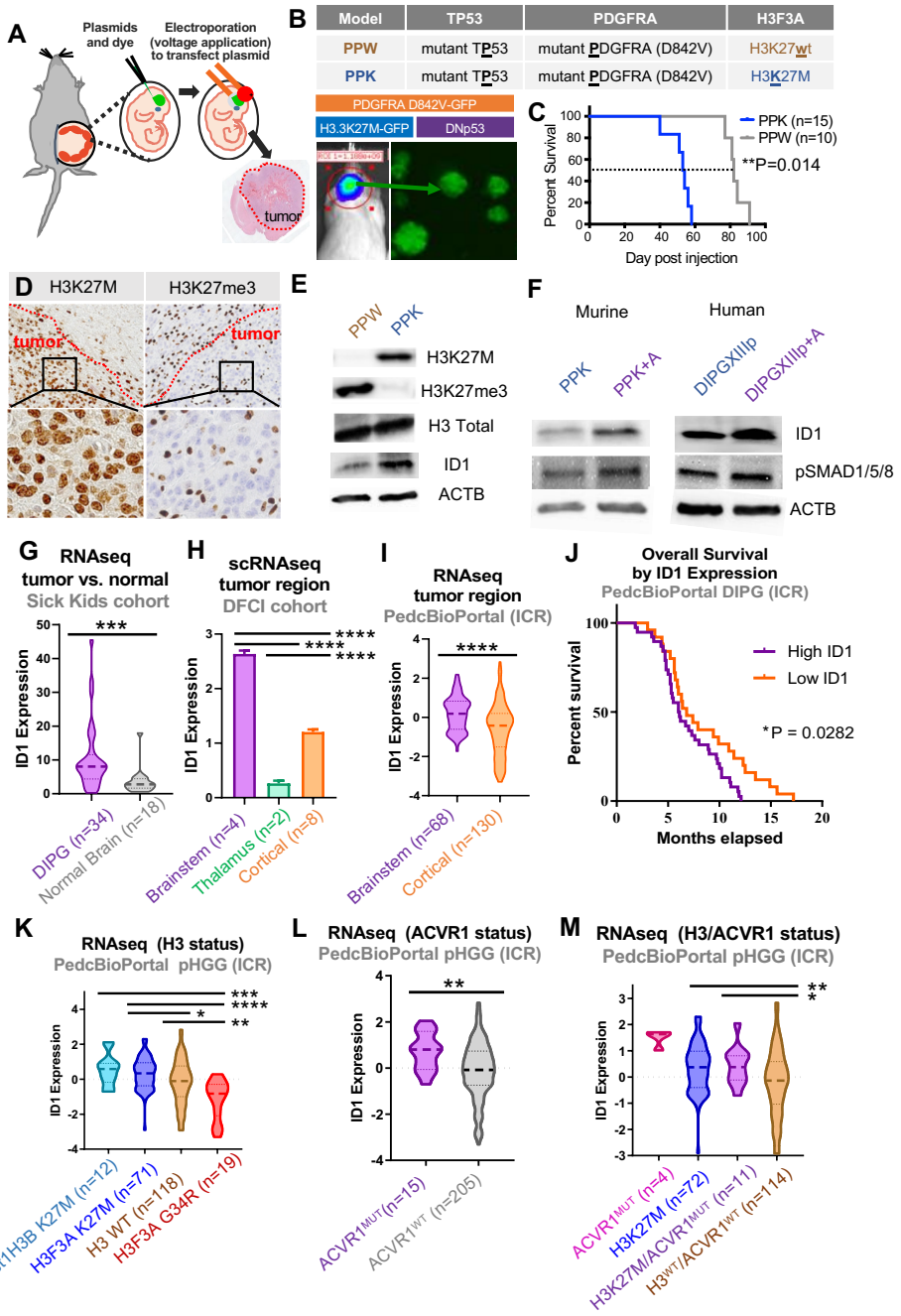

Fig. 1. Elevated expression of *ID1* in DIPG population. (A) IUE-mediated H3K27M-tumor model. **(B)** PDGFRA^{MUT}-p53^{MUT}-H3^{WT} ("PPW") and PDGFRA^{MUT}-p53^{MUT}-H3K27M ("PPK") tumors are generated by IUE. Tumor growth is monitored by in vivo bioluminescence imaging and primary neurosphere cell cultures are generated by dissociation of tumor tissue. **(C)** Survival

bioRxiv preprint doi: https://doi.org/10.1101/2021.05.10.443452; this version posted May 11, 2021. The copyright holder for this preprint (which was not certified by peer review) is the author/funder, who has granted bioRxiv a license to display the preprint in perpetuity. It is made available under aCC-BY-NC-ND 4.0 International license.

curve for PPW and PPK mice displays significantly reduced survival of PPK compared to PPW mice; **P=0.014, log-rank test. **(D)** IHC-stained images of PPK tumor show tumor-specific H3K27M expression and reduced H3K27me3 (representative of n=3 PPK tumors). Magnification = 10x (top row); 40x (bottom row). **(E)** Western blot (WB) of PPW and PPK primary neurospheres for assessment of H3K27M, H3K27ac and ID1 expression by H3 mutational status. **(F)** WB of murine PPK and PPK+*ACVR1*^{MUT} ("PPK+A") cells, and human DIPGXIIIp and DIPGXIIIp+*ACVR1*^{MUT} cells, for assessment of ID1 and pSMAD expression. **(G)** *ID1* expression of DIPG tissue (n=34) compared to matched normal brain tissue (n=18) from the SickKids cohort; ***P < .001, unpaired parametric t-test. **(H)** *ID1* expression by scRNA-seq from the DFCI cohort, including brainstem (n=4), thalamus (n=2) and cortex (n=8); ****P<0.0001, one-way ANOVA t-test. **(I)** *ID1* expression of DIPG tissue (n=68) compared to hemispheric pHGG tissue (n=130). Data from ICR cohort; ****P < 0.0001, unpaired t-test. **(J)** Kaplan-Meier survival curve of DIPG patients (n=66) grouped by high and low *ID1* expression. *P =0.0282, Mantel-Cox test. **(K)** *ID1* expression across *Hist1H3B (H3C2)* K27M (n=12), *H3F3A (H3.3A)* K27M (n=71), H3^{WT} (n=118) and *H3F3A (H3.3A)* G34R (n=19) DIPG tumors. Data from ICR cohort, presented in Mackay et al; *P<0.05, **P<0.01, ***P<0.001, ****P<0.0001, one-way ANOVA t-test. **(L)** *ID1* expression of pHGG tissue by *ACVR1* mutational status (n=15 ACVR1^{MUT} ; n=205 ACVR1^{WT}). Data from ICR cohort; **P<0.01, unpaired parametric t-test. **(M)** *ID1* expression of pHGG tumors with *ACVR1* mutation only (n=4), H3K27M only (n=72), H3K27M and *ACVR1* mutations (n=11) and neither mutation (H3WT/*ACVR1* WT; n=114). Data from ICR cohort; *P<0.05, **P<0.01, one-way ANOVA t-test.

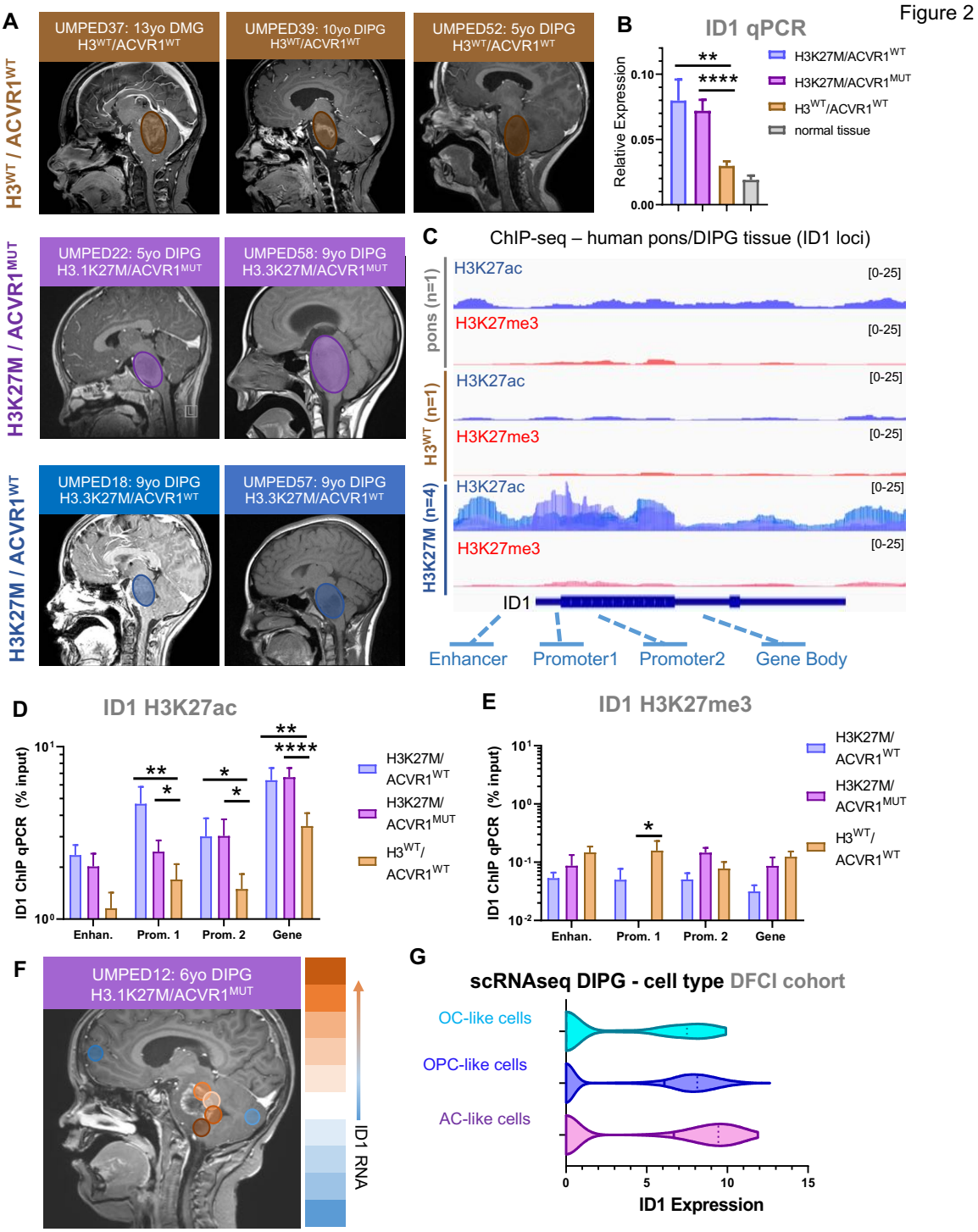

Fig. 2. *ID1* is epigenetically active in H3K27M-DIPG. (A) Multifocal DIPG tumor samples were obtained at autopsy from n=2 patients with H3K27M mutation and wildtype *ACVR1* (ACVR1^{WT}), n=2 patients with H3K27M mutation and *ACVR1* mutation (ACVR1^{MUT}) and n=3

801 patients with wildtype H3 and *ACVR1*. Circles over MRI images represent the approximate
802 region of tumor. **(B)** *ID1* expression (qPCR) for multifocal samples collected from patients in
803 (A). Data represent mean+/-SEM; **P<0.01, ****P<0.0001, one-way ANOVA t-test. **(C)** ChIP-
804 sequencing of H3K27ac and H3K27me3 deposition at the *ID1* gene locus in normal human
805 pontine tissue (n=1), $H3^{WT}$ DIPG tumor tissue (n=1) and H3K27M DIPG tumor tissue (n=1). **(D-**
806 **E)** ChIP-qPCR quantification of deposited (D) H3K27ac, and (E) H3K27me3 marks at gene
807 body elements identified in part C for the *ID1* gene. Data represent samples from patients in (A),
808 mean+/-SEM; *P<0.05, **P<0.01, ****P<0.0001, one-way ANOVA t-test. **(F)** MRI image of
809 H3K27M/$ACVR1^{MUT}$ DIPG patient with circles representing regions where samples were
810 obtained at autopsy. Color scale on right displays relative level of *ID1* expression by qPCR
811 (orange=higher *ID1* expression; blue=lower *ID1* expression. **(G)** ScRNA-seq data (DFCI, n=4
812 DIPGs) of malignant DIPG cells plotted to show ID1 expression across varying subtypes of cells
813 [oligodendrocyte-like (OC-like); OPC-like; AC-like].

Figure 3

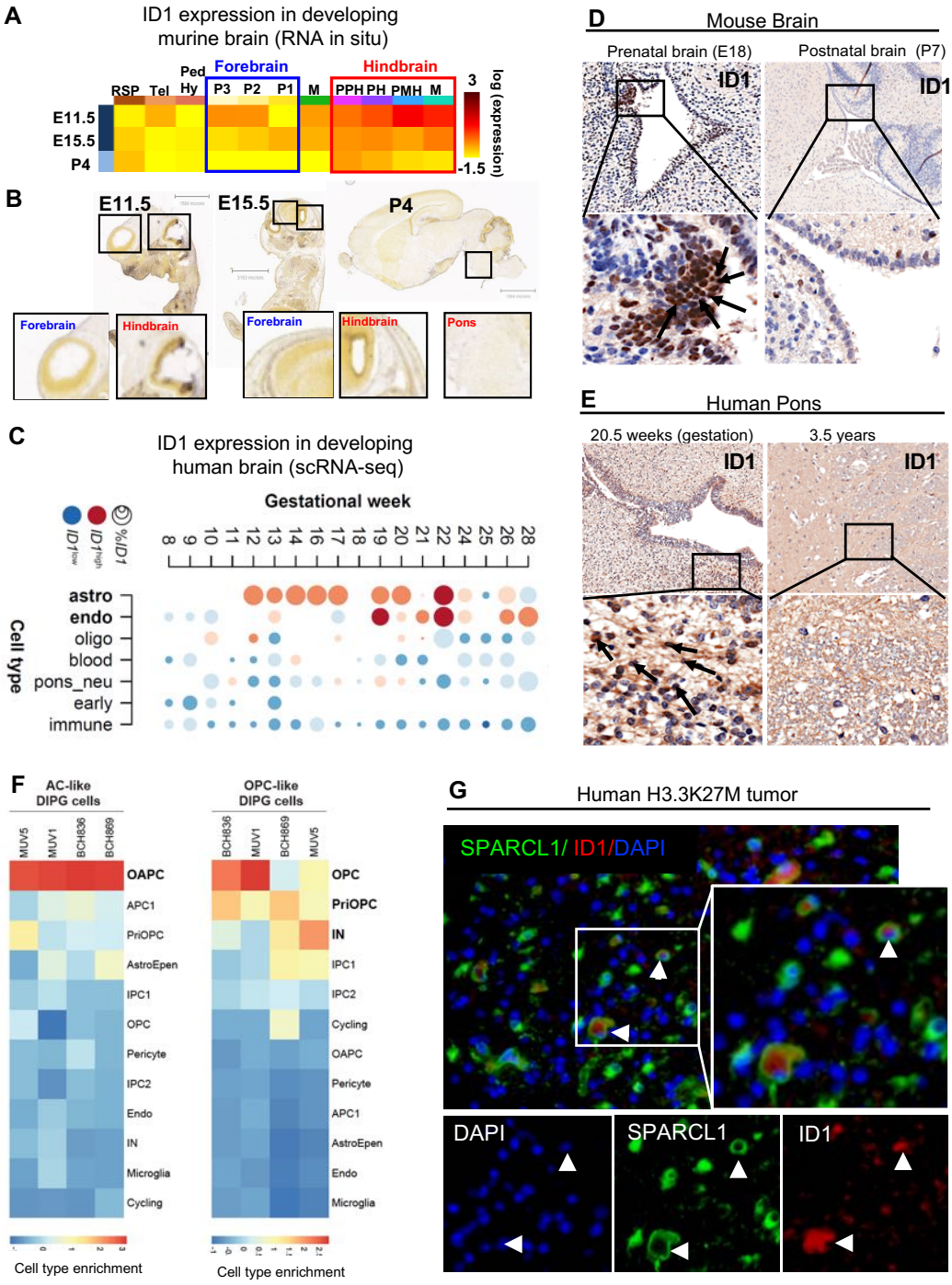

Fig. 3. ID1 expression is elevated in developing astrocyte cells in prenatal human and murine hindbrain. (A) Heat map showing relative *ID1* expression by in situ hybridization (ISH)

817 in murine brain across development. Available from: http://developingmouse.brain-map.org/. **(B)**
818 ISH of sagittal developing murine brain sections showing higher *ID1* RNA in embryonic
819 hindbrain than forebrain, and minimal *ID1* RNA in all post-natal brain [Allen Developing Mouse
820 Brain Atlas. Available from: http://developingmouse.brain-map.org/]. **(C)** Heatmap of *ID1*
821 expression across varying cell types during normal human pontine development [data from Fan
822 et al. (*25*)]. Circle size indicates the percentage of cells that express ID1 and color indicates the
823 expression level in $ID1^+$ cells (red=high expression; blue=low expression). **(D)** ID1 IHC staining
824 of normal human pontine tissue displays higher ID1 expression in cells lining the 4th ventricle at
825 20.5 weeks gestation and minimal expression in brain tissue at 3.5 years of age. **(E)** ID1 IHC of
826 normal murine pontine tissue at embryonic day 18 (E18) displays higher ID1 expression
827 compared to postnatal day 7 (P7). Magnification = 10x (top row); 40x (bottom row). **(F)** Overlap
828 of genes expressed by cell types in the developing human pons Fu et al. (*28*) in DIPG tumor cell
829 subsets. (Red=cell type marker genes enriched in DIPG cells; blue=cell type marker genes not
830 enriched in DIPG cells). **(G)** Immunostaining of SPARCL1 (green) and ID1 (red) in human
831 DIPG tissue showing co-localization of ID1 and SPARCL1 in a subset of cells (white arrow).
832 Scale bar, 20 µm. Tumor nuclei were stained with DAPI (blue). [For (A), from left to right (row
833 headings), RSP: rostral secondary prosencephalon, Tel: telencephalic vesicle, PedHy: peduncular
834 (caudal) hypothalamus, P3: prosomere 1, P2: prosomere 2, P1: prosomere 3, M: midbrain, PPH:
835 prepontine hindbrain, PH: pontine hindbrain, PMH: pontomedullary hindbrain, MH: medullary
836 hindbrain (medulla); from top to bottom (column headings), E11.5/15.5: embryonic day
837 11.5/15.5, P4: postnatal day 4].

Figure 4

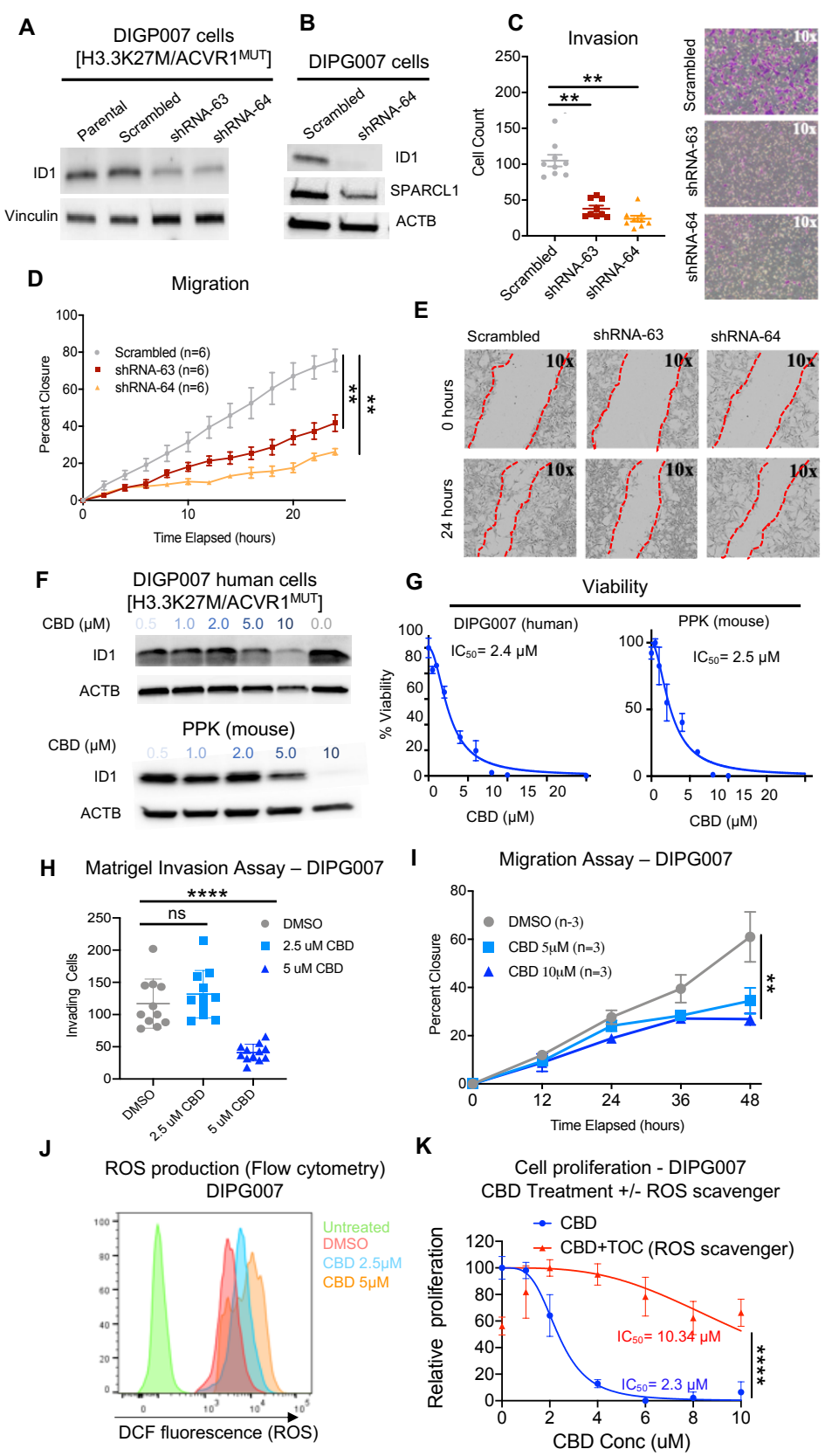

838 **Fig. 4. Genetic and Pharmacological inhibition of *ID1* decreases DIPG cell invasion and**

839 **migration. (A)** Western blot (WB) confirming *ID1* knockdown in DIPG007 cells. (B) WB
840 depicting reduction in SPARCL1 expression along with decreased ID1 expression in *ID1*-
841 knockdown DIPG007 cells. **(C)** Effect of *ID1* knockdown on invasion as measured by Matrigel-
842 coated Boyden chamber assay. Images show invading cells stained with crystal violet. Each data
843 point represents an individual image; **P < 0.01, unpaired parametric t-test. **(D-E)** Effect of *ID1*
844 knockdown on DIPG007 migration as measured by scratch assay, quantified as percent wound
845 closure. Images show representative scratch at 0 and 24 hours outlined in dotted red line.
846 Experiment was completed in triplicate and data points represent mean+/-SEM, **P < 0.01;
847 images taken with Incucyte; area measured by ImageJ. **(F)** WB for ID1 and ACTB expression in
848 DIPG007 and PPK cells treated with increasing concentrations of CBD or DMSO control. **(G)**
849 Viability of DIPG007 and PPK cells treated with increasing concentrations of CBD (0.5-20μM)
850 relative to DMSO-treated control. Experiment was completed in triplicate and data points
851 represent mean+/-SEM. **(H)** DIPG007 cells were treated for 2 days with DMSO (control), 2.5μM
852 or 5μM CBD and invasion was measured by Matrigel-coated Boyden chamber. Each data point
853 represents an individual image, mean+/-SEM; ****P < 0.0001, unpaired parametric t-test. **(I)**
854 Effect of CBD treatment (5-10μM) on DIPG007 migration as measured by scratch assay,
855 quantified as percent wound closure. Experiment was completed in triplicate and data points
856 represent mean+/-SEM, **P < 0.005, two-way ANOVA t-test. **(J)** Histogram showing increase
857 in DCF (ROS) with increasing doses of CBD. **(K)** Production of ROS mediates the inhibitory
858 activity of CBD through ID1. DIPG007 cells were treated for 72 hours with vehicle (DMSO) or
859 different concentrations of CBD (10, 8, 6, 4, 2, 1 μM) in the presence and absence of 50 μM
860 TOC. IC_{50} was 2.3μM for CBD treatment alone and 10.34μM for CBD + TOC; ****P < 0.0001,
861 two-way ANOVA t-test. Cell proliferation was measured using XTT assay.

Figure 5

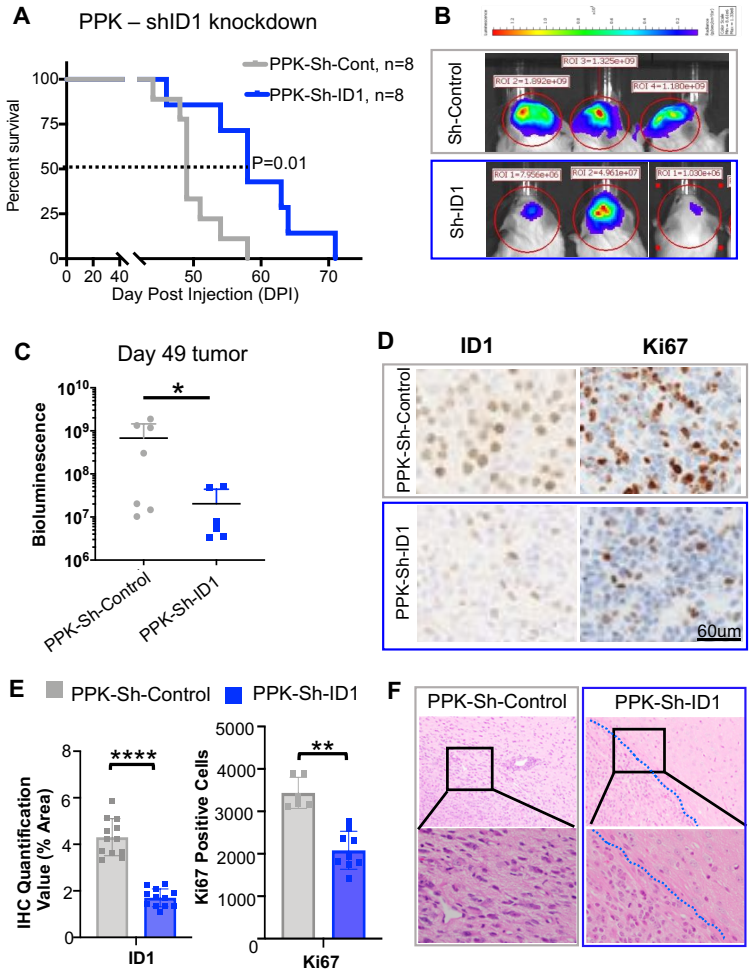

Fig. 5. Genetic targeting of ID1 decreases cell viability and slows murine tumor growth in PPK IUE tumor model. (A) Standard Kaplan-Meier survival plot reveals notable increase in survival for PPK-Sh-ID1 [*PDGFRA*-, *TP53*- and H3K27M-mutant with ID1 knockout (n=8)] mice with median survival 58 days post-IUE injection compared to PPK-Sh-control (n=8) mice with median survival of 49 days; P=0.01, Log-rank test. **(B)** Representative bioluminescence images of PPK-Sh-control tumors and PPK-Sh-ID1 (representative from n=8), 49 days after IUE injection, displaying lower average luminescence in the PPK-Sh-ID1 group than in the PPK-Sh-control. **(C)** IUE PPK bioluminescence tumor monitor growth data with statistical significance between PPK-Sh-control and PPK-Sh-ID1 groups 49 days after IUE injection. *P<0.05, one-way ANOVA t-test. (**D**) IHC analysis of ID1 and Ki67 expression in tumors from PPK-Sh-ID1 and

872 PPK-Sh-control mice. Images representative of each experimental cohort. Magnification=40x.
873 **(E)** IHC quantification for PPK-Sh-control and PPK-Sh-ID1 mice for ID1 and Ki67 expression
874 levels. **P=0.0065 and ****P ≤ 0.0001, one-way ANOVA t-test. Data points include 3 animals
875 per treatment group and 4 images per animal. Data represent the mean+/-SEM. **(F)** Images of
876 IUE-generated PPK-Sh-Control and PPK-Sh-ID1 tumor borders for assessment of tumor cell
877 invasiveness. Magnification = 10x (top row); 40x (bottom row).

Figure 6

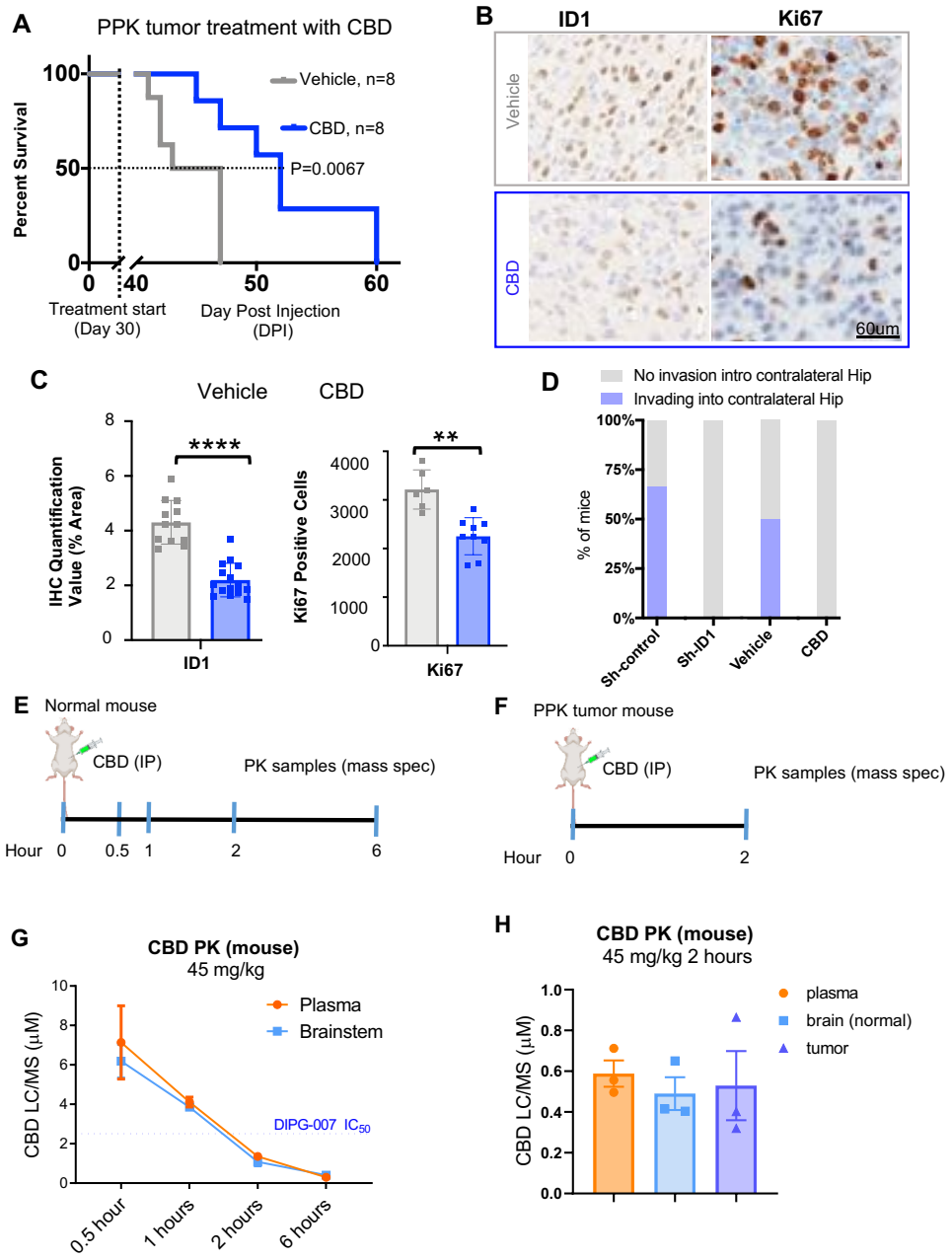

878 **Fig. 6. Therapeutic inhibition of ID1 with CBD decreases ID1 expression and improves**

879 **survival of PPK tumor-bearing mice. (A)** Survival curve for PPK mice shows that median

880 survival for control condition was 45 days post-IUE injection (n=8) and 55 days for CBD

881 condition (15 mg/kg, n=8). **P<0.005, Log-rank test. **(B-C)** IHC analysis and quantification of

882 tumor images reveals that CBD treatment reduced expression of ID1 and Ki67 compared to

883 vehicle-treated tumors (representative of n=3 tumors); **P=0.0065 and ****P ≤ 0.0001,
884 Dunnett's multiple comparisons test. N=3 animals per treatment group and 4 images per animal.
885 Data represent the mean+/-SEM. Magnification=10x. **(D)** Analysis of tumor invasion in tumor-
886 bearing mice (n=3 mice per group) with genetic (sh-ID1) or pharmacologic (CBD) ID1
887 knockdown. Invasion was defined as tumor infiltration into the contralateral hippocampus (Hip).
888 **(E)** Timeline for pharmacokinetic (PK) liquid chromatography (LC)/mass spectrometry (MS)
889 analysis of CBD treatment by intraperitoneal (IP) injection in normal mouse plasma and
890 brainstem. **(F)** Timeline for PK mass spec analysis of CBD treatment by IP injection in PPK
891 mouse plasma, normal brain and tumor. **(G)** PK analysis results for normal (non-tumor-bearing)
892 mice treated with 45 mg/kg CBD (n=3 mice per time point). Data represent CBD concentrations
893 as determined by LC/MS for the plasma and brainstem; mean+/-SEM. Blue dashed line
894 represents estimated IC_{50} of CBD for DIPG007 cells. **(H)** PK analysis results for n=3 PPK mice
895 treated with 45 mg/kg CBD. Data represent CBD concentrations as determined by LC/MS for
896 the plasma, normal brain and tumor; mean+/-SEM.

Figure 7

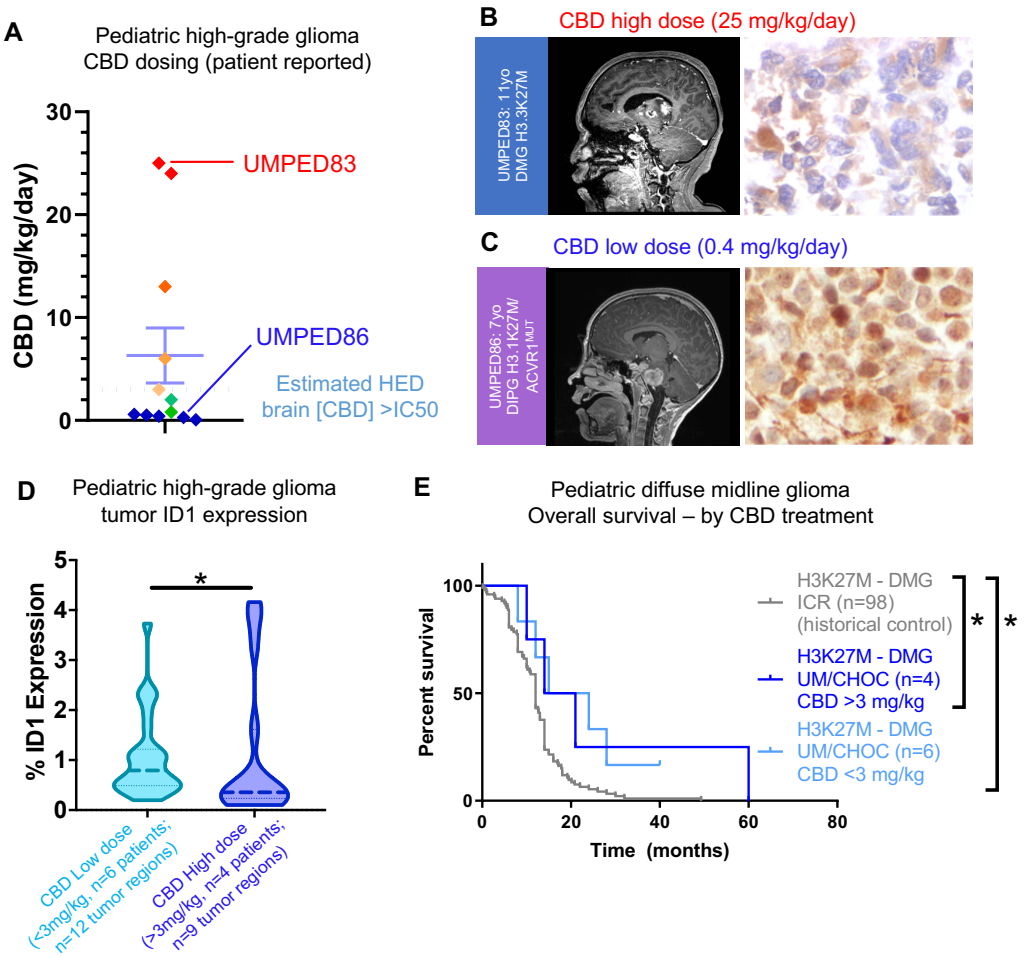

Fig. 7. Treatment of human pHGG patients with CBD. (A) Plot representing the CBD dosing range (mg/kg/day) in human patients, including one high (UMPED83) and one low (UMPED86) dose of CBD, as indicated by red and blue lines. **(B-C)** IHC-stained tumor tissue from DIPG patients (B) UMPED83 treated with CBD (25 mg/kg) and (C) UMPED86 treated with CBD (0.4 mg/kg/day) during treatment course for assessment of ID1 expression. IHC images representative of n=3 images taken using Aperio ImageScope, magnification=40x. **(D)** ID1 IHC analysis and quantification of human DIPG tumor samples with low (n=6) and high dose (n=4) of CBD; *P=0.0388, Mann-Whitney U test. **(E)** Survival of H3K27M-mutant tumor patients treated with CBD from higher than 3mg/kg (n=4) and lower than <3mg/kg (n=6) with historical control (n=98).

Figure 8

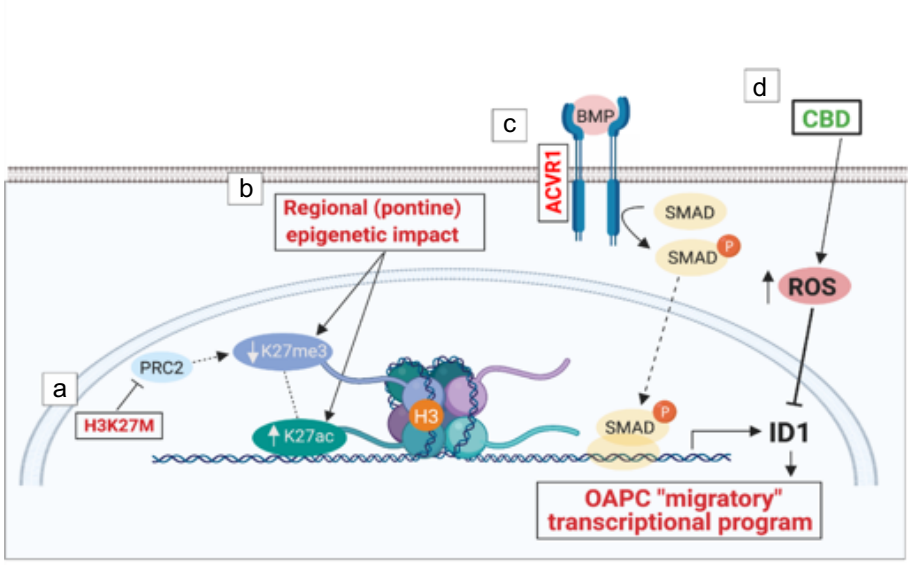

Fig. 8. Proposed model of ID1 activation in DIPG with H3K27M and ACVR1 mutations and its inhibition with CBD. The proposed model is made up of the following sub-sections: (a) H3K27M inhibits PRC2, leading to global decreases in H3K27me3 and subsequently allowing for increased H3K27ac. (b) Regional or tissue-specific factors and/ or (c) constitutively activating *ACVR1* mutations increase *ID1* expression via SMAD protein signaling. We propose that ID1 expression replicates the developing cell subtype OAPC transcriptional program, which promotes migration. (d) ID1 expression is reduced by CBD treatment, which partially acts through increasing intracellular levels of reactive oxygen species (ROS). Image created with BioRender.

920 **Supplementary Materials**

921 **Supplementary Methods**

922 **Whole exome and transcriptome sequencing (Sick Kids, Toronto)**

923 Use of patient tissues was approved by the Hospital for Sick Children (Toronto) Research
924 Ethics Board. WES/WGS (accession EGAS00001000575) from DIPG samples plus matched
925 normal was using DNA extracted from fresh-frozen tissues as described (*13*). Fresh-frozen tissue
926 was used for total RNA extraction with the RNeasy mini kit (QIAGEN, CA, USA). 34 DIPG and
927 17 normal brain samples passed quality control. The TruSeq Stranded Total RNA Library Prep
928 with Ribo-Zero Gold Kit (Illumina, CA, USA) was used and paired end sequencing generated
929 with Illumina HiSeq 2500 machines (accession EGAD00001006450) (*51*). Sequencing quality
930 was confirmed with FastQC v0.11 (http://www.bioinformatics.babraham.ac.uk/projects/fastqc/).
931 Reads were quality trimmed with Trimmomatic (*52*) v0.35 before being aligned with RSEM (*53*)
932 v1.2 to human transcriptome build GRCh37 v75. Gene expression was quantified FPKM.
933

934 **Whole exome and transcriptome sequencing of tumor/normal tissue (University of**
935 **Michigan)**

936 Clinically integrated sequencing was performed according to previously published
937 methodology (*54, 55*). For living patients with DIPG/HGG, the PEDS-MIONCOSEQ study was
938 approved by the Institutional Review Board of the University of Michigan Medical School and
939 all patients or their parents or legal guardians provided informed consent (written assent if >10
940 years). For deceased patients, parents were consent for research autopsy and brain tumor/normal
941 banking separately from the MIONCOSEQ protocol. Tumor (FFPE or frozen) and normal
942 (cheek swab or blood, when available) samples were submitted for whole exome (paired tumor

943 and germline DNA) and transcriptome (tumor RNA) sequencing. Nucleic acid preparation, high-
944 throughput sequencing, and computational analysis were performed by the Michigan Center for
945 Translational Pathology (MCTP) sequencing laboratory using standard protocols in adherence to
946 the Clinical Laboratory Improvement Amendments (CLIA) (*56*).

947

948 **Analysis of tumors from Institute for Cancer Research (ICR)**

949 Whole exome and transcriptome sequencing data from 1067 pediatric high grade gliomas
950 (pHGGs) (compiled from the Jones lab, ICR London, Cancer Cell 2017) was retrieved from the
951 ICR cohort (*20*). Specimens with mRNA sequencing (n=247) were then separated by location
952 into brainstem/pons (n=68), hemispheric (n=130), and midline (n=49). PHGGs of the brainstem
953 were considered DIPGs. Of the 68 DIPGs from the ICR cohort, 2 did not have survival data and
954 were removed. Overall survival was defined from day of diagnosis to death of patient. High *ID1*
955 expression was defined as having a z-score greater than 0.2 (n=38), and low *ID1* expression as
956 less than 0.2 (n=25).

957

958 **In Utero Electroporation (IUE) and generation of primary cell lines from IUE tumors**

959 PiggyBac transposon plasmids containing *PDGFRA* mutation, *TP53* mutation, *H3F3A*-
960 K27M, and *H3F3A*-WT, were kind gifts from Dr. Timothy Phoenix (Cincinnati Children's
961 Hospital, Cincinnati, OH) (*57*). *In utero* electroporation was performed on isoflurane/oxygen-
962 anesthetized pregnant female mice at embryonic day E13.5 in the cortex. Subcutaneous delivery
963 of Vetergesic and Carpofen at 0.1 mg/kg and 5 mg/kg, respectively, was also provided pre-
964 emptively. Briefly, IUE were performed using sterile technique on isoflurane/oxygen-
965 anesthetized pregnant CD1 females at E13.5. Uterine horns were exposed through a 1 cm

incision and embryos were digitally manipulated into the correct orientation. Borosilicate capillaries were loaded with endotoxin-free DNA and Fast Green dye (0.05%, Sigma) for visualization. Lateral ventricles were then injected with the DNA-dye mixture using a microinjector (Eppendorf). 3-5 plasmids were injected at the same time, each at a concentration of 2 µl/µl. 1-2 µl of total solution was injected into each embryo. DNA was electroporated into cortical neural progenitors using 3 mm tweezertrodes (BTX), applying 5 square pulses at 35 V, 50 ms each with 950 ms intervals. Embryos were then returned into abdominal cavity, muscle and skin sutured, and animal monitored until full recovery. Periodically, tumor growth was monitored by IVIS as mice are treated starting 33 days post injection (dpi).

Primary cell lines with specific genetic alterations were generated from IUE-induced pediatric high grade glioma models. Mice with confirmed large tumors (bioluminescence 10^7 – 10^8 photons/s/cm^2/sr) were selected. Mice were euthanized with an overdose of isoflurane, decapitated, and brain was dissected from the skull. Brain was then placed in a Petri dish, and coronal cuts were made anterior and posterior to tumor using sterile scalpel. Tumor was identified and dissected with fine forceps and placed in a 1.5 ml tube containing 300 µl of Neural Stem Cell Media (NSC Media: DMEM/F12 with B-27 supplement, N2 supplement, and Normocin, supplemented with human recombinant EGF and bFGF at a concentration of 20 ng/ml each). Tumor was gently homogenized using a plastic pestle. 1 ml of enzyme free tissue dissociation solution was added to homogenized tumor, and then incubated at 37°C for 5 minutes. Then, cell suspension was passed through a 70 µm cell strainer, centrifuged at 300x g for 4 min. Supernatant was decanted, and pellet resuspended in 7 ml of NSC media. Solution was then plated onto a T25 tissue culture flask, and placed in tissue culture incubator at 37°C with atmosphere of 95% air and 5% CO_2. After 3 days, neurospheres were removed and re-plated into

989 a T75 tissue culture flask. Cells were then maintained in NSC media appropriately. No
990 mycoplasma testing regimen was performed on murine cell lines as they are early passage tumor-
991 derived cells. If frozen, cells were cultured for 2 to 3 passages (2 weeks) following thawing for
992 experiments.
993
994 **Mint-ChIP-sequencing of tumor tissue**
995 Analyses for the two classical histone modifications H3K27ac and H3K27me3
996 representing accessible and repressed chromatin states were performed as part of a MiNT-ChIP
997 analysis for 9 tumor samples of DIPG patients in comparison to a control tissue sample of
998 healthy pons according to the protocol published by Buenstro et al., 2013. Up to 50 mm^3 snap
999 frozen tumor tissue was digested with 2.5 mg/ml collagenase IV (Sigma-Aldrich, Germany) and
1000 dissociated via the gentleMACS Dissociator (Miltenyi, Germany). Subsequent
1001 immunoprecipitation for H3K27Ac and H3K27me3 was performed with 5 µg of ChIP-grade
1002 antibodies, monoclonal murine anti-H3K27Ac (MABI0309, ActiveMotif, Belgium) and a
1003 polyclonal rabbit anti-H3K27m3 (Merck Millipore, Germany).
1004 Over 50 mio reads were sequenced in 50 bp paired-end sequencing runs on a NovaSeq
1005 6000 system (NGS Core Facility, University Hospital, Bonn, Germany) and demultiplexed as
1006 described by Buenstro et al., 2013 (Core Unit Bioinformatics Data Analysis, University Hospital
1007 Bonn, Germany). Reads were aligned against the human reference genome hg19 by Bowtie2
1008 (v2.4.2). Tag directories of piled up reads were created using HOMER (v4.11)
1009 makeTagDirectory and visualized makeUCSCfile with the -fsize 5e8 option.
1010
1011 **Native ChIP-qPCR**

1012 Protocol for native ChIP-qPCR was adapted from previously described methods, and
1013 optimized for frozen human tissue (*58*). Antibodies against H3K27ac (2 μl, cat# 07360,
1014 Millipore Sigma), H3K27me3 (1 μg, cat# 07449, Millipore Sigma), and control IgG (2 μg
1015 Cat#12370, Millipore Sigma) were used for immunoprecipitation.
1016 Quantitative-PCR was performed per below methods, using 1μl of eluted ChIP DNA. Primers
1017 for *ID1* enhancer and promoter region target sites were predicted based on H3K27ac peaks
1018 observed in the four H3K27M DIPG tumor tissue samples analyzed via ChIP-sequencing in
1019 main Figure 2C. For a complete list of primers used in ChIP-qPCR, see Supplementary Table S1.
1020 NCBI RefSeq hg19 was used as reference genome (*43*). Enrichment at target sites was quantified
1021 using the percent input method as has been previously described (*59*). Gene expression was
1022 quantified relative to GAPDH using the comparative C_T method as previously described (*60*).
1023 For a complete list of primer sequences used in qPCR for gene expression, see Supplementary
1024 Table S2.
1025
1026 **Analysis of developing murine brain**
1027 Call sets from the ENCODE portal (https://encodeproject.org/) were downloaded with the
1028 following identifiers: ENCSR691NQH, ENCSR428GHF, and ENCSR066XFL. ChIP-
1029 Sequencing peaks were quantified using EaSeq (http://easeq.net) (*61*). Graphic depictions of
1030 H3K27ac peaks at the *ID1* locus were generated using IGV browser (*62*). ID1 in situ
1031 hybridization (ISH) data and images from the 2014 Allen Developing Mouse brain Atlas
1032 (http://developingmouse.brain-map.org/) were downloaded and analyzed.
1033
1034 **ScRNA-seq analysis from developing brain and H3K27M-mutant DIPGs**
1035

1036 Single-cell gene expression data and their clusters in the developing brain were obtained
1037 from GSE133531 (mouse pons), GSE120046 (human pons, gestational week 8-28), and
1038 GSE144462 (human cortex, gestational week 21-26). Raw mouse expression data was
1039 normalized to counts-per-million for each cell. Cells were assigned to clusters based on the joint
1040 clustering of cells from all four developmental stages (E15.5, P0, P3, P6). 1,792 cells were
1041 removed due to missing cluster assignments and Id1 expression was analyzed in the remaining
1042 22,682 cells. Analysis of normalized human pontine expression data was restricted to 4,228 cells
1043 that were detected across 18 gestational time points in the pons (>=3 cells per gestational week).
1044 Normalized human expression data for H3K27M-mutant DMGs was obtained from GSE102130.
1045 Tumor cells with an astrocytic differentiation (AC-like), oligodendrocytic differentiation (OC-
1046 like), and OPC-like program were determined using stemness- and lineage scores from Filbin et
1047 al. (*19*) and *k*-means clustering. Mann-Whitney U (MWU) tests were used to identify for each
1048 patient genes that separate AC-like and OPC-like cells. Cell type enrichments were calculated
1049 using significant marker genes (cell type set A) and full summary statistics obtained from
1050 differential marker gene analysis (enrichment score=z-transformed median -log10 MWU P
1051 values). Functional enrichment analysis of marker genes was performed using the Enrichr web
1052 service (*63*) and top 200 marker genes (sorted by MWU P-value).
1053

1054 **DIPG immunohistochemistry (IHC) staining and quantification**

1055 Mouse PPK tumor and human DIPG paraffin embedded tissue were sectioned and sent to
1056 Dr. Daniel Martinez (Department of Pathology, Children's Hospital of Philadelphia, PA) for ID1
1057 and Ki67 staining. Briefly, ID1 antibody (Biocheck BCH-1) was used to stain formalin-fixed
1058 paraffin embedded tissue slides. Slides were rinsed in 2 changes of xylene for 5 min each then

1059 rehydrated in a series of descending concentrations of ethanol. Slides were treated with .3%
1060 H2O2/methanol for 30min. and then treated in a pressure cooker (Biocare Medical) with 0.01M
1061 Citrate buffer pH 7.6. After cooling, slides were rinsed in 0.1M Tris Buffer and then blocked
1062 with 2% fetal bovine serum for 5 min. Slides were then incubated with ID1 antibody at a 1:25
1063 dilution overnight at 4 degrees C. Slides were then rinsed and incubated with biotinylated anti-
1064 Rabbit IgG (Vector Laboratories BA-1000) for 30min at room temp. After rinsing, slides were
1065 incubated with the avidin biotin complex (Vector Laboratories PK-6100) for 30 min at room
1066 temp. Slides were then rinsed and incubated with DAB (DAKO Cytomation K3468) for 10 min
1067 at room temp. Slides were counterstained with hematoxylin, then rinsed, dehydrated through a
1068 series of ascending concentrations of ethanol and xylene, then coverslipped. Ki67(SP6) antibody
1069 (Abcam ab16667) was used to stain formalin-fixed, paraffin–embedded tissue. Staining was
1070 performed on a Bond Max automated staining system (Leica Microsystems). The Bond Refine
1071 staining kit (Leica Microsystems DS9800) was used. The standard protocol was followed with
1072 the exception of the primary antibody incubation which was extended to 1 hour at room
1073 temperature. Ki67 was used at 1:400. Antigen retrieval was performed with E2 (Leica
1074 Microsystems) retrieval solution for 20min. After drying, slides were scanned at 20x
1075 magnification with an Aperio CS-O (Leica Biosystems) slide scanner and images were viewed
1076 using the Aperio ImageScope software. An individual blinded to the experiment captured five
1077 random images from each IHC slide at 10X magnification. Quantification of images for precent
1078 positive area were measured by ImageJ software.
1079
1080 **Human cell cultures**

1081 Primary H3.3K27M-mutant cell line DIPG007 was obtained from Dr. Rintaru Hashizume
1082 from (Northwestern University, Chicago, IL) who obtained them originally from Dr. Angel
1083 Carcaboso (Hospital Sant Joan dr Deu, Barcelona, Spain). DIPG-XIII was obtained from Dr.
1084 Michelle Monje (Stanford University, Stanford, CA). PBT-29 was obtained from Dr. Nicholas
1085 Vitanza,(Seattle Children's, Seattle, WA). Immortalized human embryonic kidney 293
1086 (HEK293) cells were obtained from Dr. Sriram Venneti (University of Michigan, Ann Arbor,
1087 MI). Cells were cultured for 2 to 3 passages (2 weeks) following thawing for experiments.
1088
1089 *DIGP007, DIPGXIIIp and PBT-29 cells*
1090 DIPG007, DIPGXIIIp and PBT-29 cells were cultured in TSM N5 media: 250 ml DMEM (1X,
1091 Cat#11995065, Gibco); 250 ml NeuroBasal-A Medium (1X, Cat#0888022, Gibco); 5 ml HEPES
1092 (1M, Cat#15630080, Gibco); 5 ml Sodium Pyruvate (100mM, Cat#11360070, Gibco); B-27
1093 Supplement without Vitamin A (50X, Cat #12587010, Gibco); 5 ml MEM NEAA (100X,
1094 Cat#11140050, Gibco); 5 ml Antibiotic-Antimycotic (100X, Cat#15240062, Gibco); 250 µl
1095 Heparin Solution (Cat#07980, STEMCELL Technologies); 10 µl human PDGF-AA every 3 days
1096 (10 ng/ml, Cat#10016, Shenandoah Biotechnology); 1 ml Normocin (Cat#antnr1, InvivoGen); 10
1097 µl human PDGF-BB every 3 days (10 ng/ml, Cat#10018, Shenandoah Biotechnology); 20 µl
1098 FGF every 3 days (20 ng/ml, Cat#10018B, PeproTech); 20 µl EGF every 3 days (20 ng/ml,
1099 Cat#10047, PeproTech). For adherent conditions, FBS was diluted in media to 10%. For
1100 neurosphere culture, FBS was not added. At each passage, cells were dissociated using StemPro
1101 Accutase (Cat#A1110501, Gibco).
1102

1103 *Human Embryonic Kidney 293 (HEK293) cells*

1104 HEK293 cells were cultured in: 500 ml DMEM (1X, Cat#11995065, Gibco); 333 µl Gluta-Max
1105 (200 mM, Cat#25030081, Gibco); 1 ml Normocin (Cat#antnr1, InvivoGen). FBS was diluted in
1106 media to 10%. At each passage, cells were dissociated using StemPro Accutase (Cat#A1110501,
1107 Gibco).

1108

1109 **ShRNA-mediated gene silencing by lentiviral transduction of cultured cells**

1110 ShRNA-mediated gene silencing for DIPG007, HEK293, or NHA cell cultures was
1111 performed by lentiviral transduction with pGIPZ shRNAs (Dharmacon, GE) targeting *ID1*
1112 (Clone ID's V2LHS_133263, V2LHS_133264) or scrambled control (Cat#RHS4346). A map of
1113 this vector is provided in Supplementary Figure S15. Protocol for lentiviral transduction was
1114 modified from the University of Michigan Vector Core as follows. 24 hours prior to
1115 transduction, cells were split into 6-well tissue culture plates at a density that they would reach
1116 approximately 60% confluency the following day. The next day, media was aspirated and
1117 replaced with 1.35 ml of fresh media. Then, 0.15 ml of 10x viral supernatant was added, along
1118 with 2.5 µl of 4mg/ml Polybrene (Cat#G062, ABM). Plate was then rocked gently on shaker to
1119 evenly distribute virus and Polybrene. Cells were then placed in cell incubator at 37°C for
1120 approximately 24 hours. Exact time was dependent on when cells began expressing GFP, which
1121 was contained in the lenti-vector.

1122

1123 **Western Blotting**

1124 Western blotting was performed using antibodies against ID1 (1:1000, Cat#133104,
1125 Santa Cruz Biotechnology), Vinculin (1:10000, Cat#700062, Invitrogen), H3K27M (1:500,

1126 EMD, Cat#ABE419), H3K27me3 (1:500, EMD, Cat#07-449) and ACTB (1:10000, Cat#A2228,
1127 Sigma-Aldrich), Secondary antibodies biotinylated horse anti-mouse IgG (Cat#BA2000, Vector
1128 Laboratories), HRP goat anti-rabbit IgG (Cat#PI1000, Vector Laboratories), and m-IgG$_k$ BP-
1129 HRP (Cat#sc516102, Santa Cruz Biotechnology) were used. Chemiluminescent blots were
1130 imaged and processed using the FluroChem M system (ProteinSimple, San Jose, CA).
1131

1132 **Cannabidiol treatment studies in vitro**

1133 Treatment was performed as previously described (*12*). 3,000 primary DIPG007 and PPK
1134 cells were plated in 96-well plates and incubated for 24 hours. The next day, cells were treated
1135 with different doses of cannabidiol (CBD) cat # 90080 (Cayman Chemical). After 72 hours, in
1136 vitro cell viability was monitored by XTT Cell Proliferation Assay kit (Cayman Chemical).
1137

1138 **Invasion assay**

1139 Invasion assays were performed using growth factor-reduced matrigel invasion chambers
1140 with 8 uM pores (Cat #354483, Corning) as described in previously published work (*50*).
1141 Seeding density and incubation time was optimized for each cell line. FBS was used as
1142 chemoattractant. Invading cells were stained with crystal violet. To count invading cells,
1143 transwell membranes were viewed underneath an inverted microscope at 10x magnification, and
1144 four pictures were taken at random locations to get an average sum.
1145

1146 **Migration (scratch) assay**

1147 Migration assays were performed following a previously published protocol with slight
1148 modifications (*64*). Cells were seeded in 6-well plates, and grown to approximately 80%

1149 confluence. Scratches were made using a 200 μl pipette tip, and migration was then monitored
1150 using the IncuCyte® live-cell analysis system (Sartorius, Ann Arbor, MI). Images were analyzed
1151 using ImageJ's MRI Wound healing tool (http://dev.mri.cnrs.fr/projects/imagej-
1152 macros/wiki/Wound_Healing_Tool). Percent closure was calculated as [($Area_{t=0} - Area_t$) /
1153 $Area_{t=0}$]*100.
1154
1155 **Proliferation and viability assays**
1156 Cell viability was quantified using the MTT Cell Proliferation Assay Kit (Cat#ab211091,
1157 ABCAM), following manufacturer instruction for adherent cells. For proliferation, cells were
1158 seeded in 96-well plates and monitored for confluence using the IncuCyte® live-cell analysis
1159 system (Sartorius, Ann Arbor, MI).
1160
1161 **Implantation of DIPG007 cells and bioluminescence imaging**
1162 *Implantation of mouse cells*
1163 Male and female NSG™ mice were obtained from Jackson Labs (Bar Harbor, ME) and
1164 were 6-10 weeks of age at the start of surgery. All animal studies were conducted according to
1165 the guidelines approved by the Institutional Animal Care & Use Committee (IACUC) at the
1166 University of Michigan. Mice were anesthetized with injection of 120 mg/kg ketamine and 0.5
1167 mg/kg dexmedetomidine. Hair above scalp was shaven, disinfected with iodine, and a 1 cm
1168 incision was made above scalp to expose cranium. The periosteum was removed with scalpel.
1169 Next, a 0.6mm burr hole was drilled 2 mm right of midline and 0.2 mm anterior to the bregma
1170 with the Ideal Micro Drill (MD-1200 120V) from Braintree Scientific Inc. Mice were placed in a
1171 Mouse/Neonatal Rat Adaptor stereotactic frame (#51615) from Stoelting. A 10 ul syringe

1172 (#7635-01) fitted with 33-gauge needle (#7762-06) from Hamilton, was filled with cell
1173 suspension (15,000 cells per uL) and penetrated 3 mm into brain tissue. After waiting two
1174 minutes, one microliter of cell suspension was injected over one minute and needle was slowly
1175 removed after waiting 3 minutes after injection. Incision was closed with 4-0 nylon and mouse
1176 was given 1 mg/kg atipamezole for reversal and monitored for recovery. Mice were monitored
1177 for symptoms of morbidity, including impaired mobility, scruffed fur, hunched posture, ataxia,
1178 and seizures.

1179 *Bioluminescence imaging*

1180 Mice were imaged using IVIS Spectrum #2 machine at the Center for Molecular Imaging
1181 at the University of Michigan Core Facility. Mice were injected with 160 mg/kg D-luciferin
1182 (#115144-35-9) from Gold Biotechnology and anesthetized with 2% isoflurane. 10 minutes after
1183 luciferin injection, mice were placed into machine in a prone position and bioluminescence was
1184 measured. Mice were imaged until peak signal was obtained for each mouse. Tumor
1185 bioluminescent signal is measured in radiance (photons) ($p/s/cm^3/sr$) in a circular region of
1186 interest (ROI) over the cranium of each mouse with Living Image Software (PerkinElmer Inc).
1187

1188 **CBD treatment studies in murine IUE PPK model**

1189 Mice harboring IUE-generated PPK HGG tumors were treated with CBD when tumors
1190 reached logarithmic growth phase (minimum 2×10^6 photons/sec via bioluminescent imaging).
1191 Mice litters from each experimental group were randomized to treatment with: (A) 15 mg/kg
1192 CBD (10% CBD suspended in Ethanol, 80% DPBS, 10% Tween-80) and (B) control treatment
1193 (10% Ethanol, 80% DPBS, 10% Tween-80). Mice were treated 5 days/week until morbidity.
1194 Animals displaying symptoms of morbidity after treatment were euthanized for

1195 immunohistochemistry (IHC) analysis. For IHC analysis, mice were perfused with Tyrode's
1196 Solution followed by 4% paraformaldehyde fixative solution to preserve the structures of the
1197 brain. For IHC quantification (Ki67 and ID1), 3-4 random images per tumor (n=3 tumors per
1198 group) were taken at 10x magnification using Aperio ImageScope and percent positive area was
1199 calculated using ImageJ software.
1200
1201 **CBD Pharmacokinetic analysis**
1202 *Mouse PK sample procurement*
1203 CBD administration to non-tumor bearing CD1 mice and PPK tumor bearing mice for PK
1204 studies were performed by IP injection at zero time point. Timeline for CBD injection and
1205 plasma, brainstem and/or tumor collection were depicted in Fig. 7 E-F. At half, one, two, and six
1206 hours after the CBD injection, the mice were isoflurane/oxygen-anesthetized and 500 uL to 1 mL
1207 of blood was drawn from the apex of the heart within the mouse's enclosed cavity. Immediately,
1208 the withdrawn blood was centrifuged within a microvette EDTA coated conical tube for 10
1209 minutes at 10,000 RPM, and the plasma was separated and stored at -80°C until PK analysis was
1210 performed. Following the blood draw, the mouse was sacrificed and the brain, brain stem, and/or
1211 tumor were extracted separately and stored at -80°C until PK analysis was performed.
1212
1213 *Chemicals and reagents*
1214 For PK studies, CBD powder was procured from Cayman chemical USA. Liquid
1215 chromatography–mass spectrometry (LC-MS) grade acetonitrile was purchased from Sigma-
1216 Aldrich. Formic acid (98%; LC-MS grade) was obtained from Fluka. A Milli-Q water system
1217 from Millipore was used to obtain ultrapure deionized water.

1218

1219 *Sample preparation*

1220 Plasma (40 µL) was dispensed into a Fisher Scientific 96-well plate, to which 40 µL of
1221 ice-cold acetonitrile (100%) and 120 µL of internal standard solution (1000 ng/mL) were added.
1222 Next, the plate was vortexed for 10 minutes. The plate was then centrifuged at 3500 revolutions
1223 per minute (RPM) for 10 minutes at 4°C to precipitate the protein. LC–tandem mass
1224 spectrometry (LC-MS/MS) was used to analyze 5 µL of the supernatant. The plasma samples
1225 were sonicated prior to being transferred to the 96-well plates. Tissue samples were weighed and
1226 suspended in 20% acetonitrile (80% water; 1:5 wt/vol). The samples were then homogenized
1227 four times for 20 seconds each time at 6,500 RPM in a Precellys Evolution system. For LC-
1228 MS/MS analysis, the CBD in brain tissue homogenates were extracted from the samples in the
1229 same manner as the CBD in plasma. Prior to extraction, samples that were above the upper limit
1230 of qualification were diluted with the same matrix. Calibrator-standard samples and quality
1231 control samples were prepared by mixing 40 µL of blank bio matrix, 40 µL of working solution,
1232 and 120 µL of internal standard solution.

1233

1234 *Calibration curve*

1235 Analytical curves were made with 12 nonzero standards by plotting the peak area ratio of
1236 CBD to the internal standard vs the concentration. The curve was created with linear regression
1237 and weighted (1/X2). The correlation coefficient demonstrated the linearity of the relationship
1238 between peak area ratio and concentration.

1239

1240 *Liquid chromatography tandem–mass spectrometry*

1241 The concentrations of CBD were determined with a Sciex AB-5500 Qtrap mass
1242 spectrometer with electrospray ionization source, interfaced with a Shimadzu high-performance
1243 LC system. The LC-MS/MS system was controlled with Analyst Software version 1.6 from
1244 Applied Biosystems; this was also used for acquisition and processing of data. Separation was
1245 performed on a Waters Xbridge C18 column (50 × 2.1 mm ID, 3.5 µm); the flow rate was 0.4
1246 mL/min. A (100% H2O with 0.1% formic acid) and B (100% acetonitrile with 0.1% formic acid)
1247 comprised the mobile phase. The gradient began with 5% B for 30 seconds and then linearly
1248 increased to 99% B at 2 minute and then reduced to 5% B at 4.1 minutes to 5.5 minutes with a
1249 runtime of 6 minutes in total. The mass spectrometer was operated in positive mode; multiple
1250 reaction monitoring was used for analysis. The Q1 m/z and Q3 m/z was 487.9 and 401.1,
1251 respectively.
1252
1253 **Statistical analyses**
1254 Statistical analyses were performed in consultation with a bioinformatician. Graphs were
1255 plotted and statistical analyses were performed using GraphPad Prism software (version
1256 7.00/8.00, GraphPad, La Jolla, CA) and Microsoft Excel. Unpaired, two-sided analysis of
1257 variance (ANOVA) followed by multiple comparison analyses were used to analyze data as
1258 indicated. Survival analyses in animals were performed using Kaplan-Meier analyses with the
1259 Log-Rank test. Data were considered significant if p values were below 0.05 (95% confidence
1260 intervals).
1261
1262 **Human studies**

1263 Informed consent was obtained for all patient samples. Two patients (CHC001 and
1264 CHC002) were enrolled on an ongoing IRB-approved prospective observational study at
1265 Children's Hospital of Colorado for children and young adults with brain tumors undergoing
1266 patient-directed medical marijuana therapy (NCT03052738). The University of Michigan cohort
1267 consisted of retrospective interviews with families of patients who underwent research autopsy.
1268 The patients all underwent research autopsy consent and were contacted to confirm use of patient
1269 details and tumor samples for this study. Patients who reported CBD therapy at any point in their
1270 care were included in this study, and CBD dosage was confirmed by pictures of CBD bottle,
1271 discussion with dispensary, etc., when possible.

1272

1273

1274

1275

1276

1277

1278

1279 **Supplementary figures**

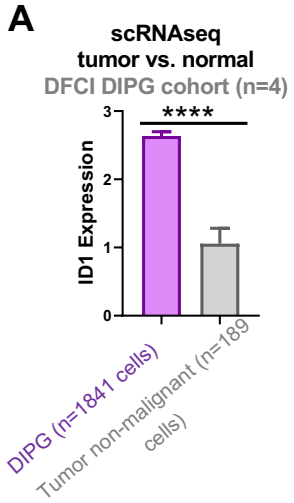

B

Figure S1

Patient ID	Age [years]	Gender	Survival [months]	Location	K27M mutation	%ID1+ cells
MUV10	9	F	8	Thalamus	H3F3A	6%
MUV1	4	F	>22	Thalamus	H3F3A	9%
BCH1126	10	F	>8	Pons	H3F3A	35%
BCH869	7	F	10,5	Pons	H3F3A	51%
MUV5	2,5	M	>19	Pons	HIST1H3B	56%
BCH836	5	F	3,5	Pons	H3F3A	69%

1280 **Supplementary Figure S1. *ID1* expression in DIPG by cell malignancy and tumor location.**

1281 **(A)** *ID1* expression of DIPG tumor by cell malignancy from the Dana-Farber Cancer Institute

1282 (DFCI) DIPG cohort (n=4 patients). ID1 expression was compared between malignant DIPG

1283 cells (n=1841) and non-malignant tumor cells (n=189) from single-cell RNA-seq (scRNA-seq)

1284 data. Data represent mean +/- SEM; ****P<0.0001, unpaired parametric t test. **(B)** *ID1* is

1285 frequently (35-69%) expressed in pontine DIPG cells and rarely (6-9%) expressed in thalamic

1286 DMGs.

Figure S2

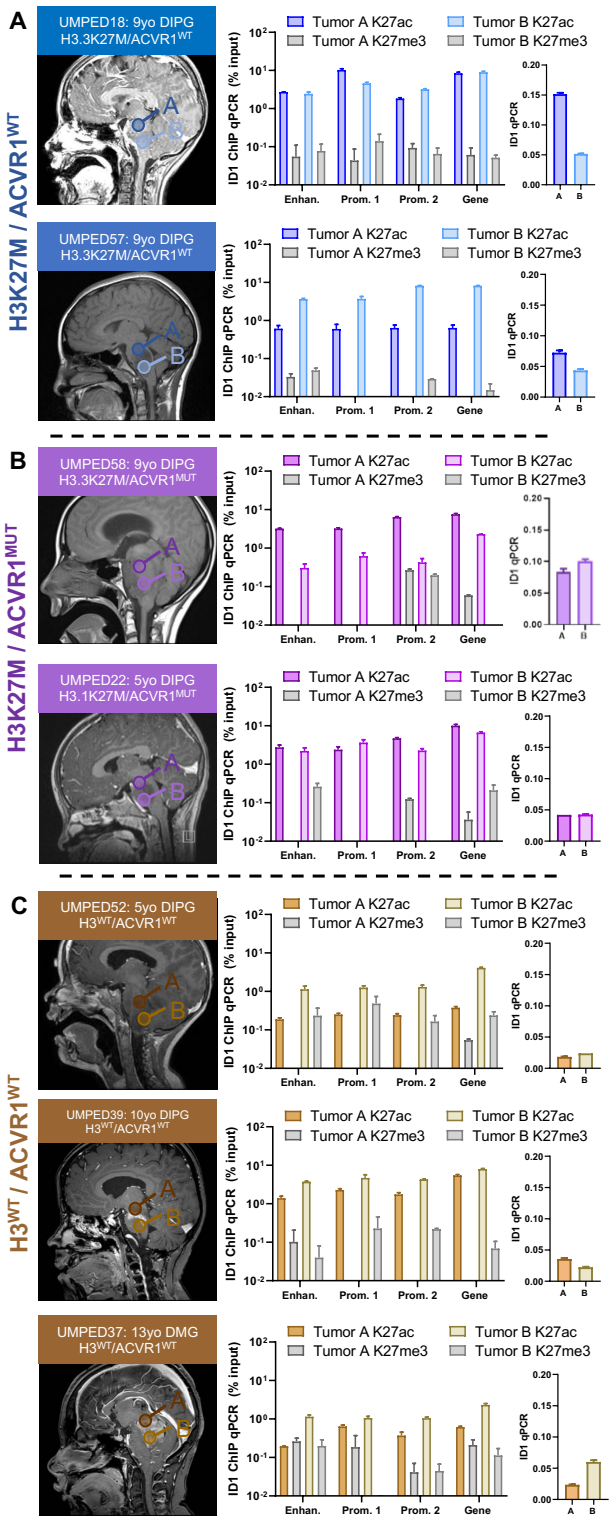

Supplementary Figure S2. Multifocal ChIP-qPCR analysis of *ID1* expression in human DIPG. (A-C) [Left panel]: Multifocal DIPG tumor samples (2 per tumor) were obtained at autopsy from n=2 patients with H3K27M mutation and wildtype *ACVR1* (ACVR1^{WT}), n=2

1291 patients with H3K27M mutation and *ACVR1* mutation (ACVR1^{MUT}) and n=3 patients with
1292 wildtype H3 (H3^{WT}) and *ACVR1*. Circles labeled "A" and "B" over MRI images represent the
1293 approximate region of tumor where a sample was obtained from. [Right panel]: Graphs on left
1294 represent percent relative enrichment for H3K27ac and H3K27me3 marks by ChIP-qPCR for
1295 each of the predicted *ID1* gene body elements shown in main figure 2. Graphs on right represent
1296 *ID1* expression, measured by qPCR, for the multifocal samples collected from patients in shown
1297 in left MRI images. Data represent mean +/- SEM.

1298

1299

1300

1301

1302

1303

1304

1305

1306

1307

1308

1309

1310

Figure S3

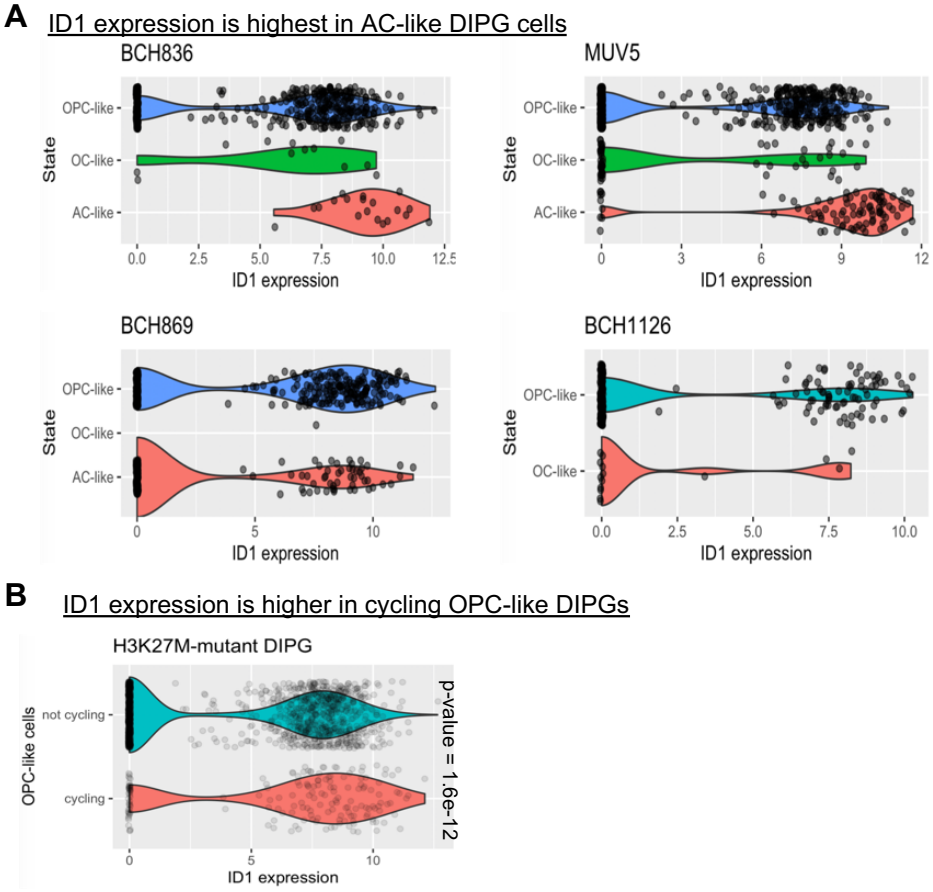

1311

1312 **Supplementary Figure S3. *ID1* expression from single cell RNA-sequencing of six different**

1313 **H3K27M-DMG patients across varying regions and malignant cell types. (A)** Violin plots

1314 depicting ID1 expression in three subtypes of H3K27M-DIPG malignant cells [Data from

1315 pontine DIPG patients in Fig. 1B]. **(B)** Violin plots depicting ID1 expression in cycling vs non-

1316 cycling malignant H3K27M-DIPG cells; $P=1.6e^{-12}$, Mann-Whitney U test. [OPC-

1317 Oligodendrocyte precursor cell; OC- Oligodendrocyte; AC- Astrocyte]. Primary data for parts

1318 (A) and (B) from Filbin et al., *Science*, 2018.

Figure S4

Supplementary Figure S4. In situ hybridization for *ID1* RNA in developing mouse brain. *ID1* RNA is high in the developing embryonic murine brain, and drastically reduced in the post-natal brain. Image credit: Allen Institute. © 2014 Allen Developing Mouse Brain Atlas. Available from: http://developingmouse.brain-map.org/

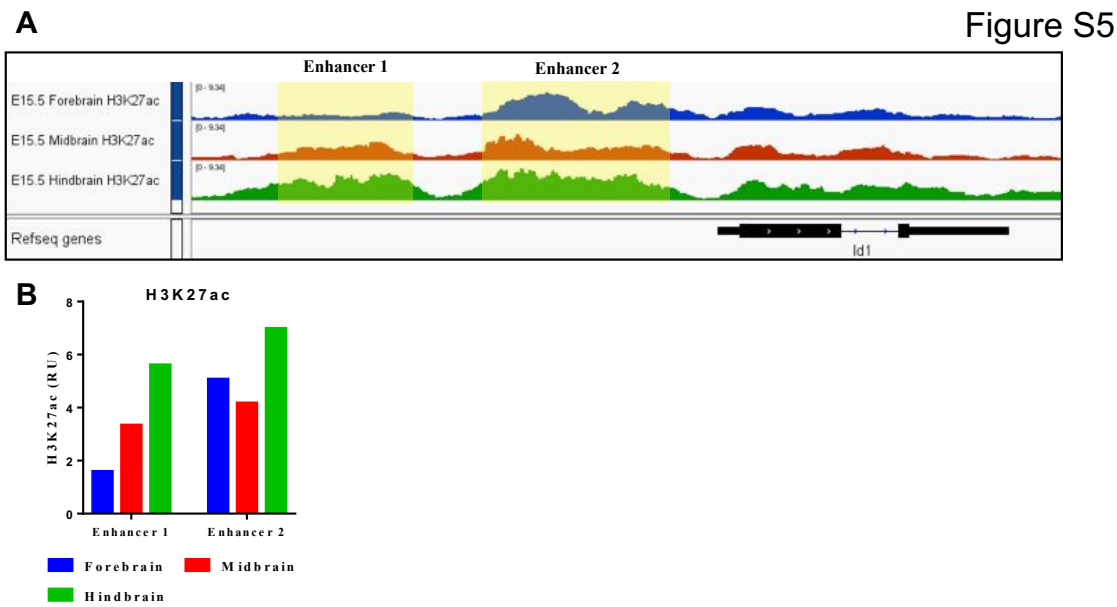

Supplementary Figure S5. H3K27ac at *ID1* locus during murine development. (A) H3K27ac peaks at the ID1 locus in E15.5 mouse brain and predicted ID1 enhancer regions [Image generated using IGV browser]. **(B)** Relative enrichment of H3K27ac at predicted ID1 enhancers in E15.5 murine brain regions. Data retrieved from ENCODE Consortium; highlighted regions quantified using EaSeq (http://easeq.net).

Figure S6

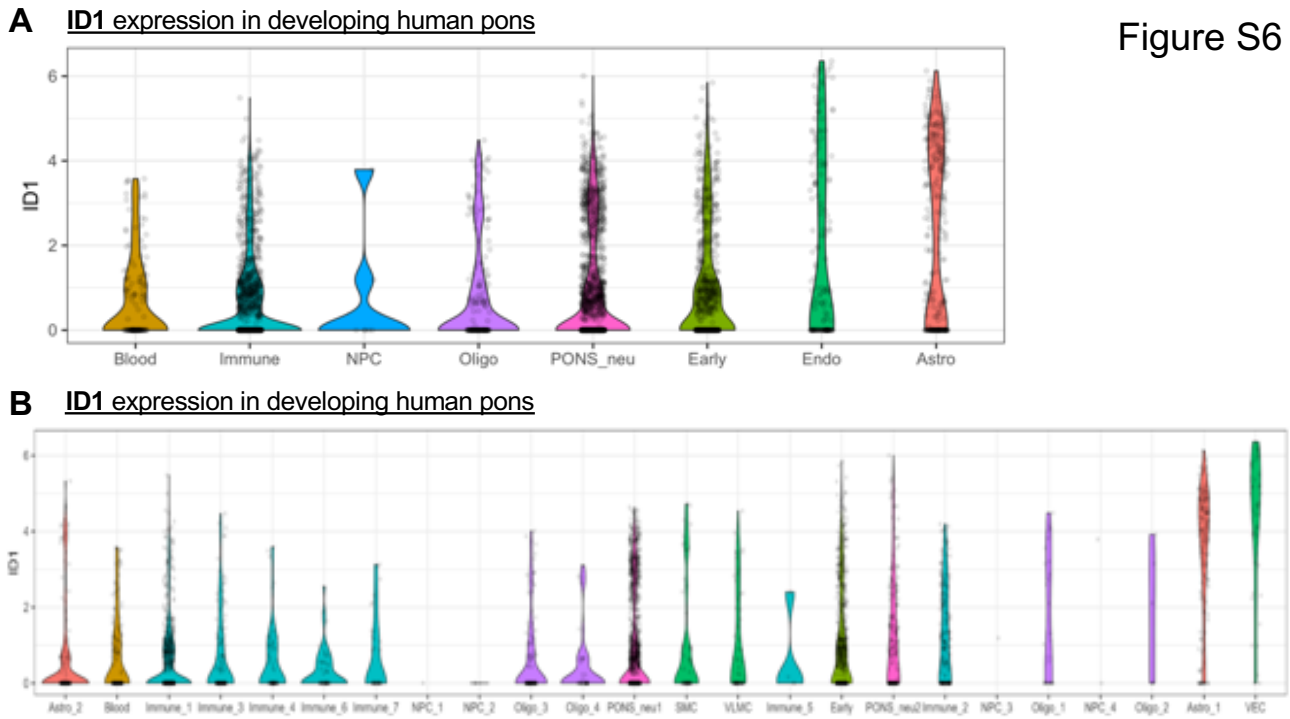

Supplementary Figure S6. *ID1* expression in varying cell types during normal murine pontine development. (A-B) Violin plots from analysis of Fan et al., *Science Advances*, 2020, depicting that AC-like cells show maximum ID1 expression during normal murine pontine development. Data points from all gestational weeks are combined for each cell type and sorted by median. [Astro- Astrocyte].

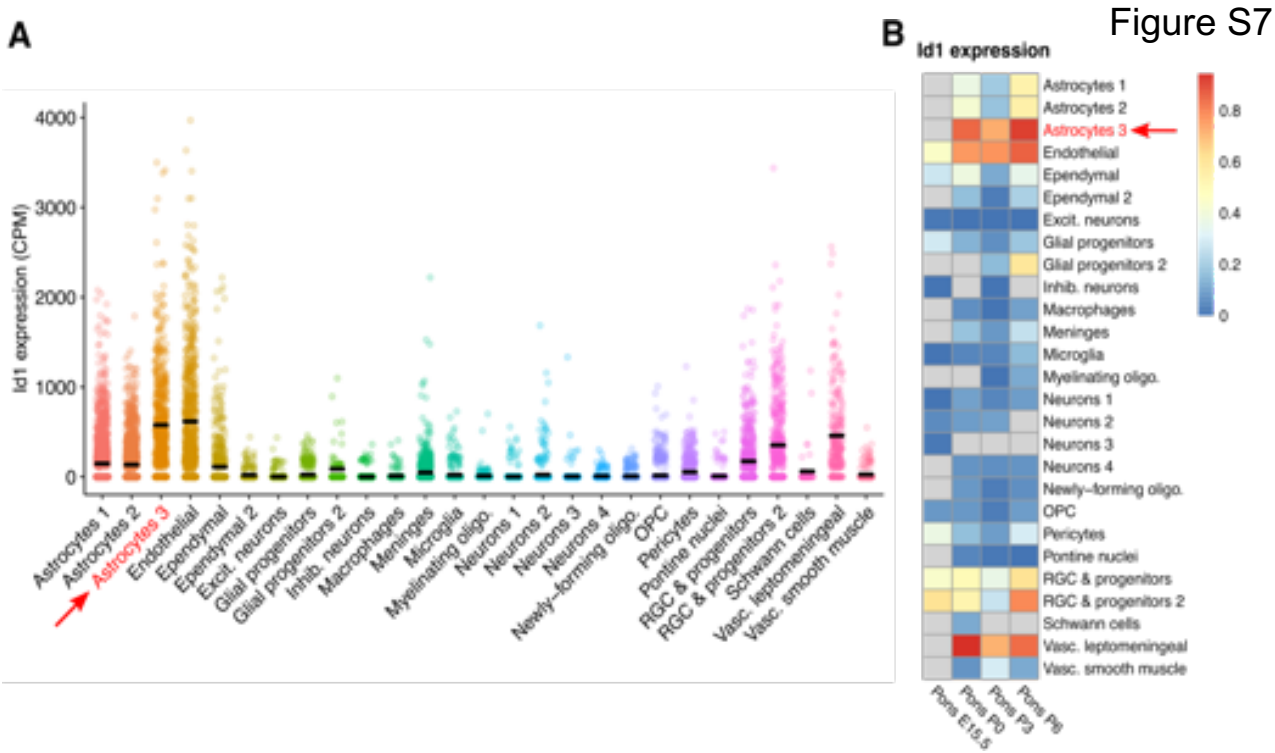

Supplementary Figure S7. ID1 expression from single-cell transcriptome analysis of varying cell types in normal developing murine pons. (A) Single-cell ID1 expression in varying cell types in normal murine pontine development. **(B)** Heatmap of ID1 expression during normal murine pontine development [E15.5- Embryonic day 15.5; P0- Postnatal day 0]. Red arrow indicates increased ID1 expression in astrocytes from P0-P6. Primary data for parts (A) and (B) from Jessa et al., *Nature Genetics*, 2019.

SPARCL1 expression is highest in AC-like DIPG cells

Figure S8

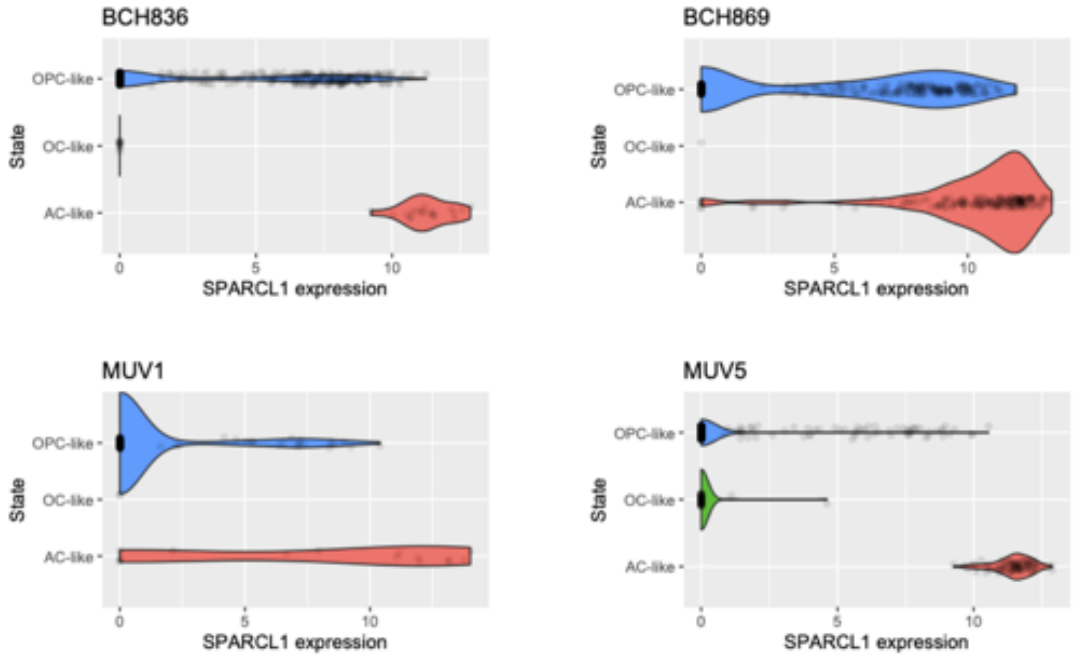

1362 **Supplementary Figure S8. *ID1* expression from single cell RNA-sequencing of four**

1363 **different H3K27M-DMG patients across varying malignant cell types.** Violin plots depicting

1364 SPARCL1 expression in three subtypes of H3K27M-DIPG malignant cells [Data from pontine

1365 DIPG patients in Fig. S1B]. Primary data from Filbin et al., *Science*, 2018. Patients MUV5,

1366 BCH836, BCH869- pontine tumors. Patient MUV1- thalamic tumor. [OPC- Oligodendrocyte

1367 precursor cell; OC- Oligodendrocyte; AC- Astrocyte].

1368

Figure S9

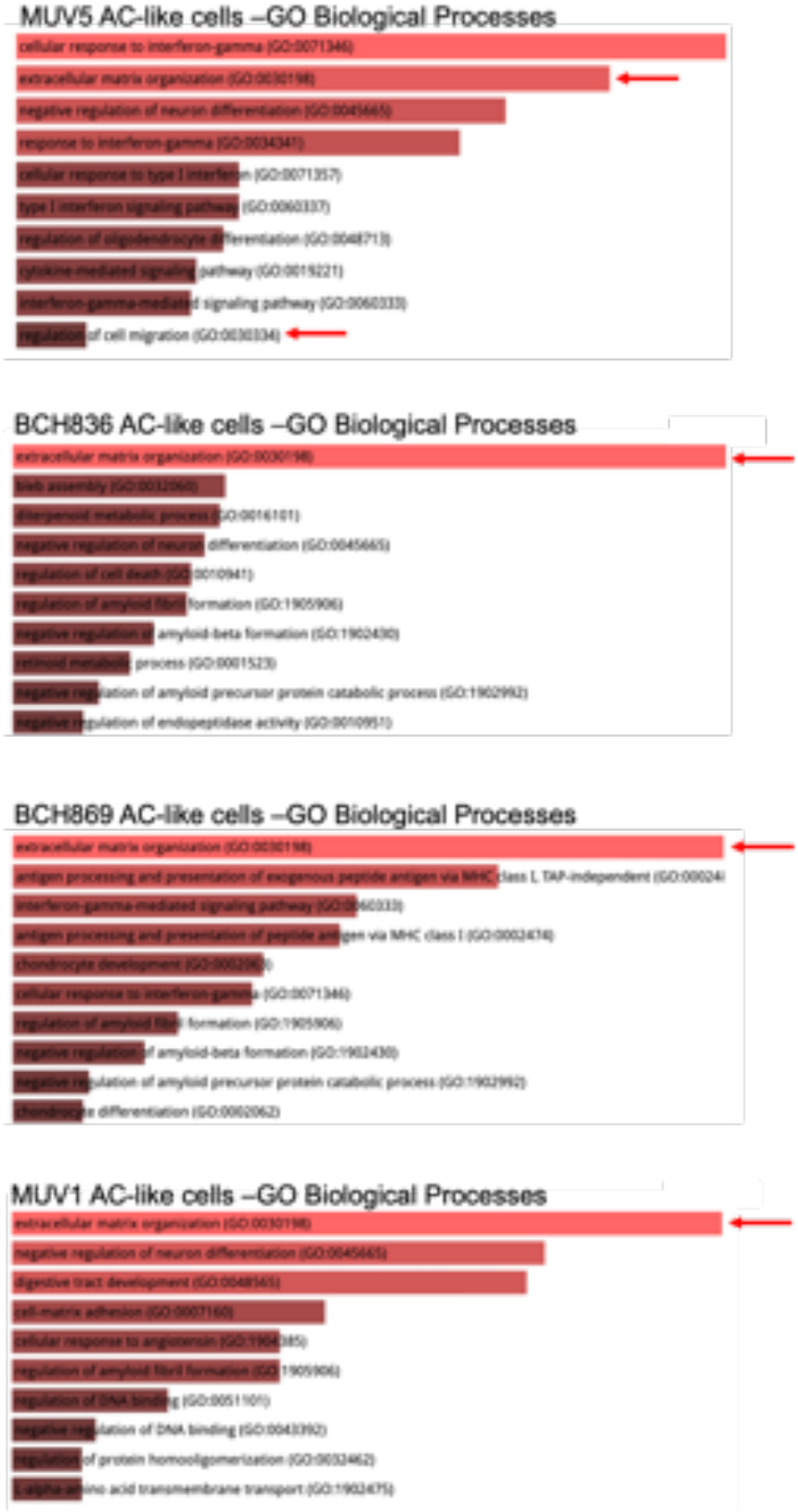

1369

1370 **Supplementary Figure S9. Gene ontology (GO) analysis of higher *ID1*-expressing AC-like**
1371 **cells from H3K27M-mutated tumor patients.** GO analysis of primary data from Filbin et al.,
1372 *Science*, 2018, demonstrates increased expression of genes related to extracellular matrix
1373 organization and regulation of cell migration in AC-like cells. Patients MUV5, BCH836,
1374 BCH869- pontine tumors. Patient MUV1- thalamic tumor.

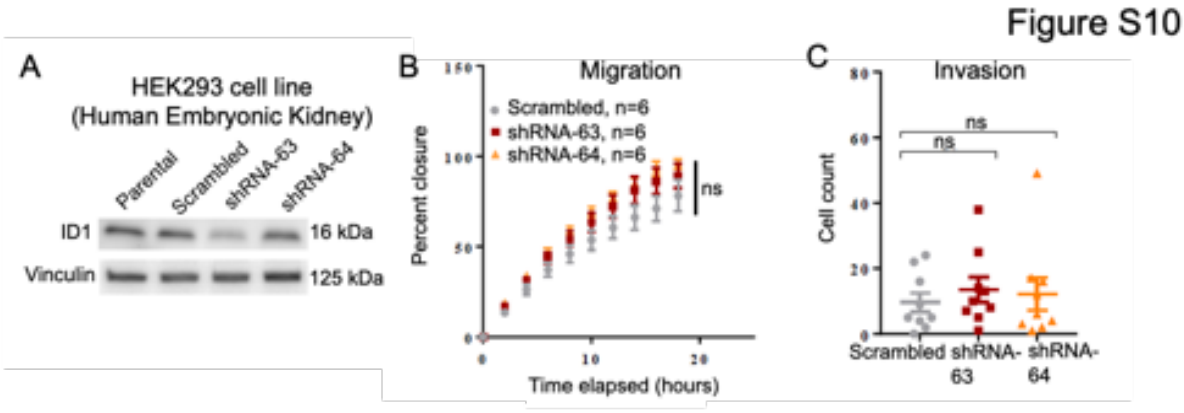

1375

1376 **Supplementary Figure S10. *ID1* knockdown in HEK293 cells. (A)** Western blot confirming
1377 *ID1* knockdown in HEK293 cells. **(B)** Effect of *ID1* knockdown on cell invasion, as measured by
1378 Matrigel-coated Boyden chamber assays. Each data point represents an individual image (4
1379 random images were taken per well). NS, P > 0.05, unpaired t test. **(C)** Effect of *ID1* knockdown
1380 on migration as measured by scratch assay. NS, P > 0.05, unpaired t test.

Figure S11

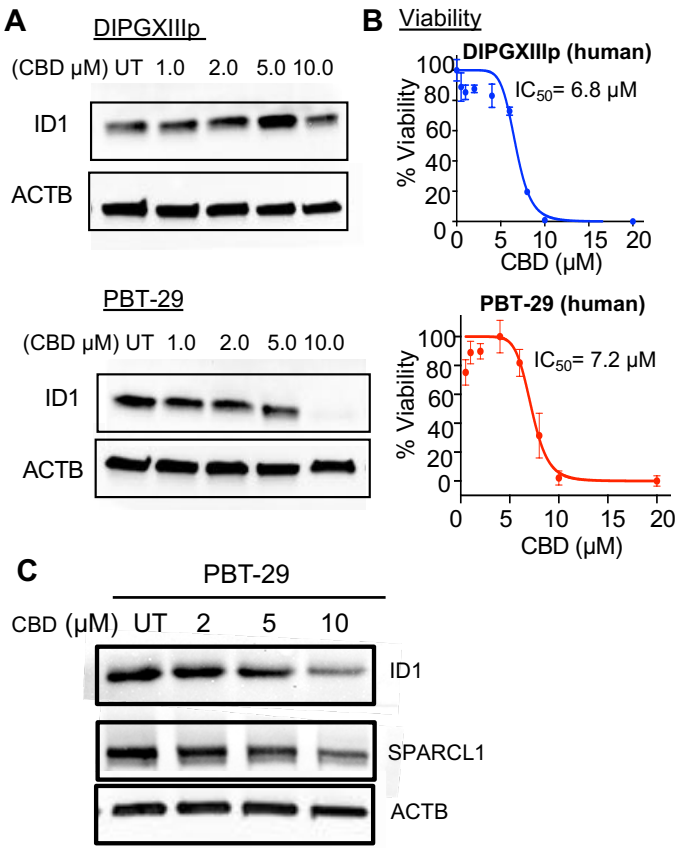

1381

1382 **Supplementary Figure S11. Impact of CBD treatment on ID1 expression in human DIPG**

1383 **cells. (A)** ID1 western blot of human DIPGXIIp and PBT-29 cells treated with increasing

1384 concentrations of CBD, or DMSO control (UT- untreated). Expression levels of ID1 and ACTB

1385 were measured. **(B)** Viability of DIPGXIIIp and PBT-029 cells treated with increasing

1386 concentrations of CBD (0.5 μM to 20 μM) relative to DMSO-treated control. Experiment was

1387 completed in triplicate and data points represent mean +/- SEM. **(C)** Western blot of ID1 and

1388 SPARCL1 expression in PBT-29 cells treated with increasing concentrations of CBD or DMSO

1389 control (UT). Experiments for all western blots were completed in triplicate.

1390

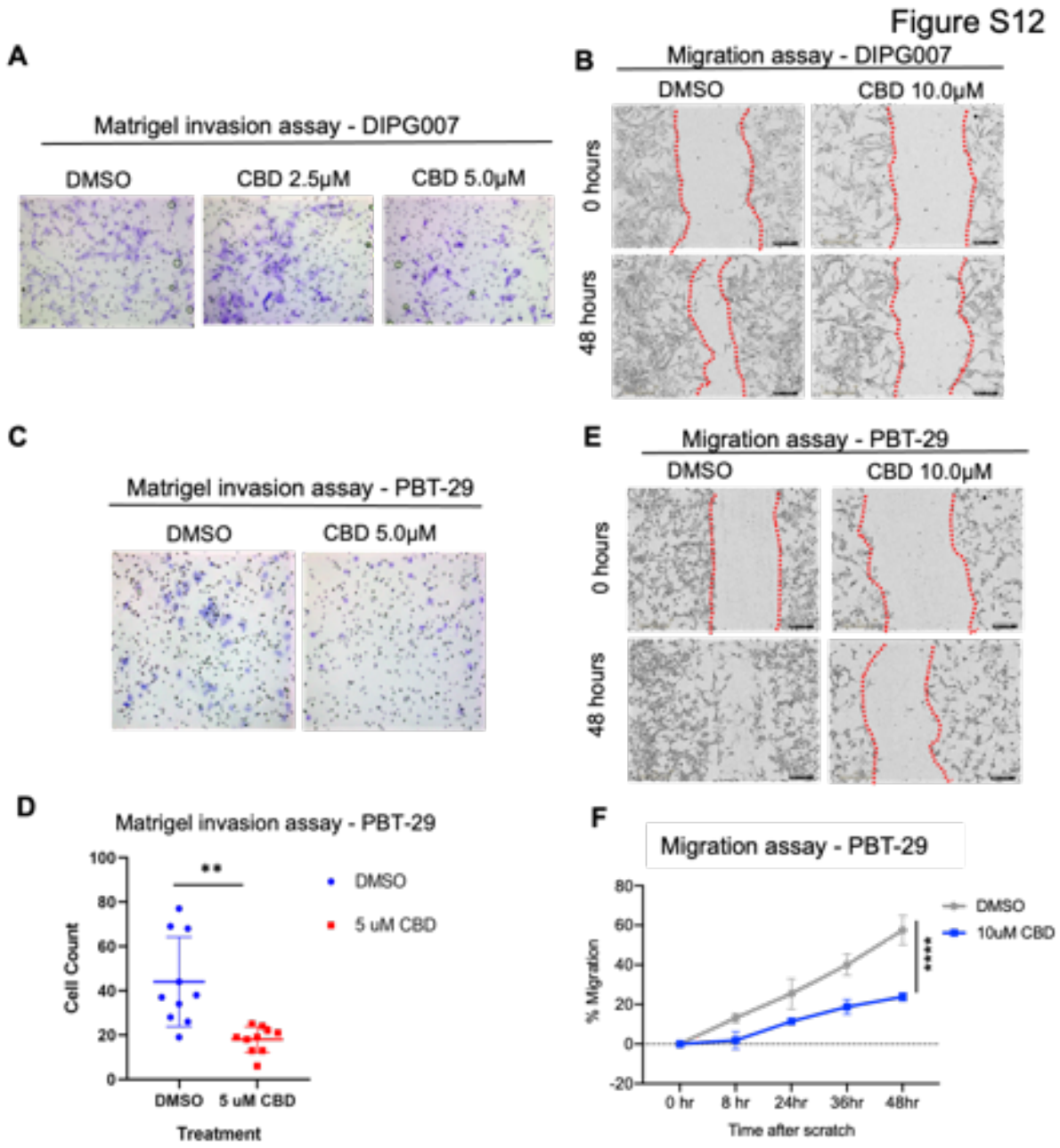

1391

1392 **Supplementary Figure S12. Effect of pharmacologic (CBD) suppression of ID1 on DIPG007**

1393 **and PBT-29 tumor cell invasion and migration. (A)** Effect of CBD treatment (2.5μM - 5μM)

1394 on invasion of human DIPG007 cells as measured by Matrigel-coated Boyden chamber assay.

1395 Images show invading cells stained with crystal violet. Number of invading cells were counted

1396 using ImageJ software. **(B)** Images displaying effect of CBD treatment (DMSO control vs

1397 10μM) on DIPG007 cell migration as measured by scratch assay. **(C)** Effect of CBD treatment
1398 (5μM) on invasion of human PBT-29 cells as measured by Matrigel-coated Boyden chamber
1399 assay. **(D)** Quantification of invading PBT-29 cells treated with either DMSO (control) or 5μM
1400 CBD shown in part C determined using ImageJ; **P<0.01, unpaired parametric t test. **(E-F)**
1401 Images displaying effect of CBD treatment (DMSO control vs 5μM) on PBT-29 cell migration
1402 as measured by scratch assay. Migration was quantified using ImageJ to determine percent
1403 wound (outlined with red dashed line) closure. Experiment was completed in triplicate. Data
1404 represent mean +/- SEM; ****P<0.0001, unpaired t test. [Magnification for all images is 20x].

1405

1406

Figure S13

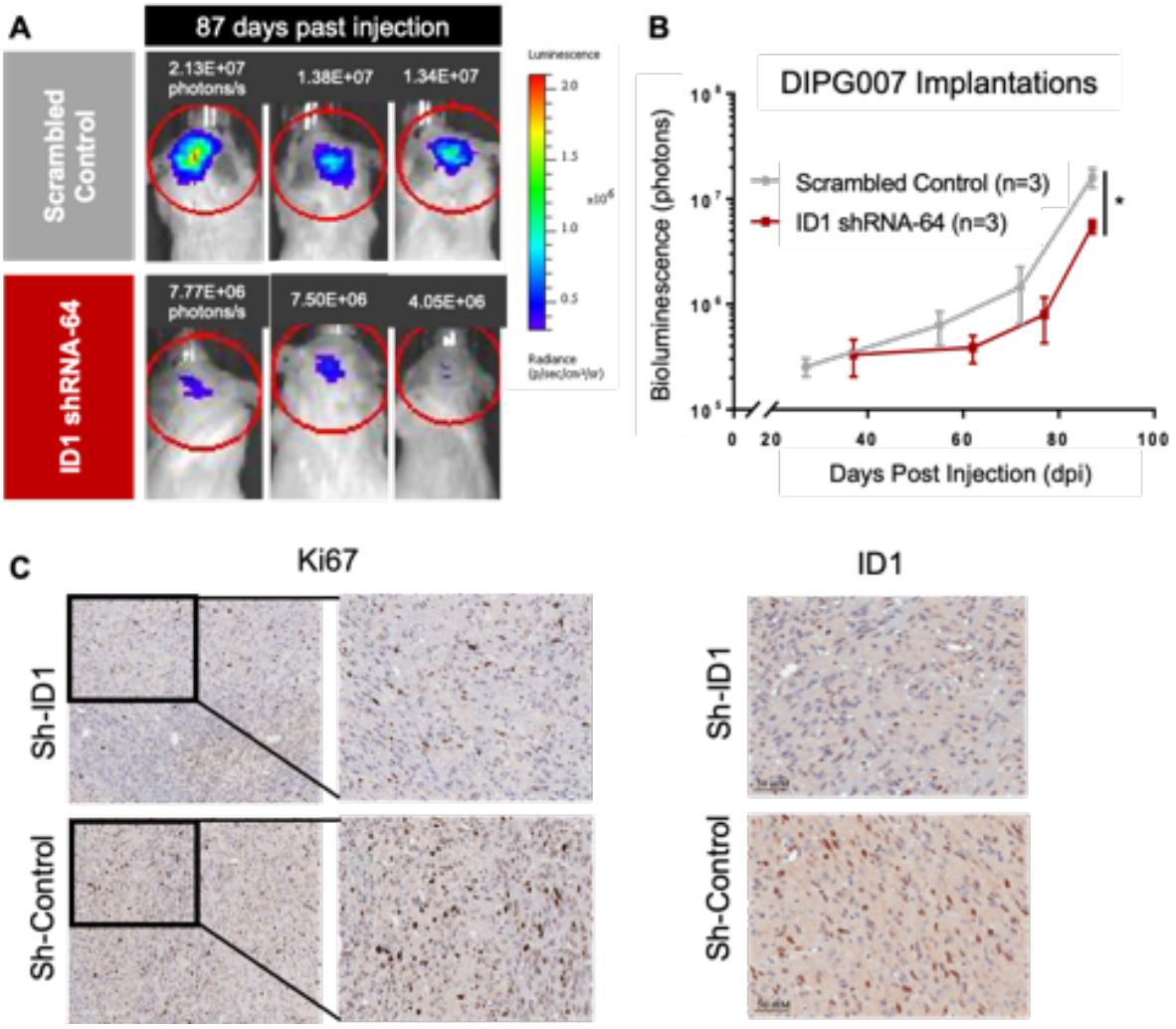

1407

1408 **Supplementary Figure S13. ID1-deficient human DIPG007 cells display slower tumor**

1409 **growth in in vivo model (A)** Representative images of bioluminescent tumors from intracranial

1410 injection of scrambled-control or ID1-shRNA DIPG007 cells at DPI-97. **(B)** Bioluminescence of

1411 intracranially-injected scrambled or ID1-shRNA DIPG007 cells over days-post-injection**. (C)**

1412 Example images of IHC staining for Ki67 (left) and ID1 (right) in a sagittal tissue section

1413 (tumors generated from implantation of DIPG007 cells). Magnification is 20x.

Figure S14

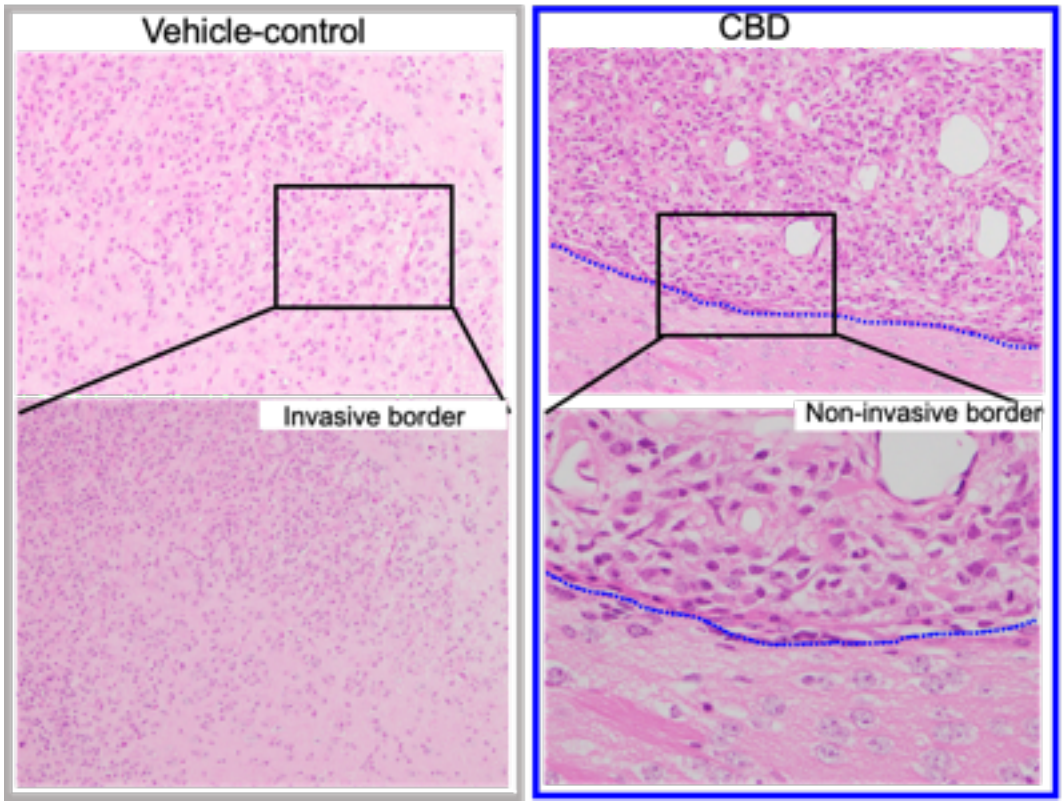

1414

1415

1416 **Supplementary Figure S14. Tumor cell invasion assessment in CBD- vs control-treated**

1417 **PPK mice.** Images of IUE-generated PPK tumor borders treated with or without CBD (DMSO

1418 vs. 15mg/kg CBD) for assessment of tumor cell invasiveness. Magnification for top row images

1419 is 10x and magnification for bottom row is 40x.

1420

1421

1422

Figure S15

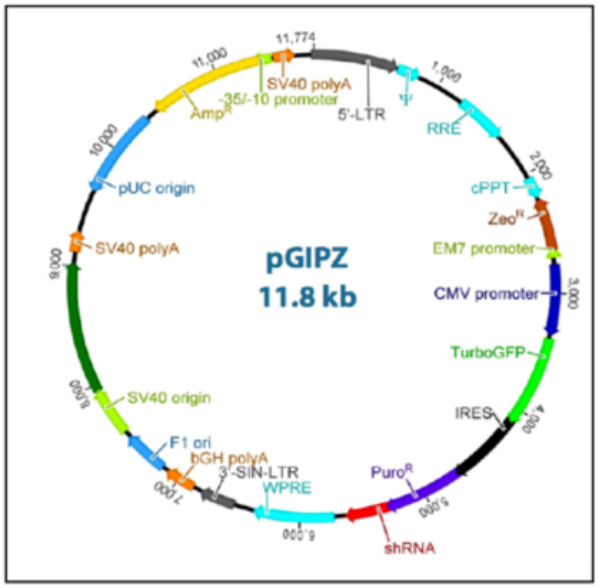

1430 **Supplementary Figure S15. Detailed vector map of pGIPZ lentiviral vector.** Lentivirus

1431 vector backbone used for ID1-targeting shRNA constructs. Image credit: Dharmacon. Available

1432 from: https://dharmacon.horizondiscovery.com/uploadedFiles/Resources/gipz-lentiviral-shrna-

1433 manual.pdf

Supplementary Table S1. Primer sequences for use in ChIP-qPCR and qPCR

Primer	Forward	Reverse	Species
ID1 Enhancer	CTGGCGTCTAACGGTCT	CTGCGGAGCTACAGTCT	Human
ID1 Promoter 1	GAGGCTGGACCTAGGAG	GAGCCACAGCTTGTCTTT	Human
ID1 Promoter 2	CTCTCATTCCACGTTCTTAAC	CTGGCGACTTTCATGATTC	Human
ID1 Gene Body	AGATCCAGATCCGACCAC	AGGTACCCGCAAGGATG	Human
PAX4 Promoter	TGGCTGAGGACTGGATCTTT	CTGGAGACAACAGCTGTCCA	Human

Primers for use in qPCR for gene expression analysis

Primer	Forward	Reverse	Species
ID1	CGAGGCGGCATGCGTTC	GGAGACCCACAGAGCACGTAAT	Human
GAPDH	CGCTCTCTGCTCCTCCTGTT	CCATGGTGTCTGAGCGATGT	Human

1434

1435 **Supplementary Table S2. Clinical details of pediatric HGG patients treated with CBD.**

Patient ID	Age	Diagnosis	Molecular	Therapies given	Time to first progression	Overall survival from Diagnosis	CBD duration/dosing/toxicity noted
CHCO01	11	DMG, H3K27M (thalamus)	H3K27M mutant	Radiation	24 months	40 months (still alive)	CBD 2.5g mg (~0.07 mg/kg/day); PO daily; CBD therapy started adjuvantly after initial radiation
CHCO02	15	DMG, H3 WT (bi-thalamic)	H3 WT; BARD1 E19* mutation; increased tumor mutational burden	Radiation; TMZ/CCNU; olaparib; pembrolizumab	14 months	26 months	CBD 50 mg (0.8 mg/kg/day); PO BID (+THC); CBD therapy started at diagnosis
UMPED18	9	DMG, H3K27M (brainstem, DIPG)	H3F3A K27M; PIK3CA E545K; TCF12 V650D	Radiation (+AZD-1775); panobinostat + everolimus	8 months	10 months	CBD 300 (13 mg/kg/day) + THC; no toxicity; PO daily; therapy started at radiation – taken until passing
UMPED22	5 yo	DMG, H3K27M (brainstem, DIPG)	HIST1H3B K27M; ACVR1 G328E	Radiation; hyper-baric O2; Re-irradiation	9 months	12 months	CBD 45 mg (2 mg/kg/day) +THC; PO BID or TID; therapy started at radiation – taken until passing
UMPED37	13	DMG, H3 WT (bi-thalamic)	H3 WT; EGFR V292L; EGFR in-frame deletion; deletion CDKN2C	Chemotherapy (thioguanine, procarbazine, lomustine, and vincristine); Radiation; osimertinib; bevacizumab	5 months	17 months	CBD 150 mg (3 mg/kg/day) after radiation -> 50 mg (1 mg/kg/day), until passing due to nausea; PO daily; therapy started at radiation – taken until passing
UMPED56	8 yo	DMG, H3K27M (brainstem, DIPG)	HIST1H3B K27M; ACVR1 R206H	Radiation; ONC201; bevacizumab	13 months	24 months	CBD (0.6 mg/kg/day) +THC; PO daily; therapy started at radiation – taken until passing
UMPED58	9 yo	DMG, H3K27M (brainstem, DIPG)	H3F3A K27M; ATRX Q119*; PPM1D G463fs; PDGFRA amplification	Radiation; multi-agent intra-arterial; ONC201	18 months	21 months	CBD (? Dose) + THC; PO or per rectum daily; therapy started at radiation – taken until passing
UMPED65	16 yo	DMG, H3K27M (brainstem, DIPG)	H3F3A K27M; TP53; PIK3CA	Radiation; ONC201; panobinostat; re-irradiation; paxilisib	16 months	24 months	CBD (0.3 mg/kg/day); PO BID/TID, intermittent early in therapy, stopped 7 months prior to passing
UMPED67	7 yo	DMG, H3K27M (thalamus)	H3F3A K27M; TP53 C277F; NF1 H2434fs	Radiation; ONC201; re-irradiation; bevacizumab	10 months	15 months	CBD (0.7 mg/kg/day) + THC; PO daily; therapy started at radiation, stopped 4-5 months prior to passing

UMPED69	4 yo	DMG, H3K27M (brainstem, DIPG)	HIST1H3B K27M	Radiation; convection-enhanced delivery (CED) trial; re-irradiation; ONC201; paxalisib	13 months	28 months	CBD 9 mg (0.5 mg/kg/day) + THC; PO TID; therapy started at radiation – taken until passing
UMPED83	11 yo	DMG, H3K27M (thalamus)	H3F3A K27M; TP53 S241C	Chemotherapy (temozolomide, irinotecan, bevacizumab); Radiation; ONC201	36 months	60 months	CBD 1500 mg (25 mg/kg/day) + THC; PO TID; therapy started at radiation, stopped one year prior to passing
UMPED86	7 yo	DMG, H3K27M (brainstem, DIPG)	HIST1H3B K27M; ACVR1 G328E; PI3KCB; PPM1D	Radiation; ONC201; Re-irradiation	6 months	8 months	CBD 3 mg (0.4 mg/kg/day); PO TID or QID; therapy started at radiation – taken until passing
UMPED97	16	Cortical anaplastic astrocytoma	H3 WT; Tp53 R342* (+germline); CDK4 gain; KRAS gain	Chemotherapy (procarbazine, CCNU, and vincristine); Radiation; irinotecan and bevacizumab	5 months	19 months	CBD 400 mg (6 mg/kg/day) after radiation, until passing due to nausea; PO twice daily (Epidiolex); therapy started at radiation – taken until passing
UMPED101	6	DMG, H3K27M (brainstem,	H3F3A K27M mutant	Radiation; ONC201; re-irradiation; bevacizumab	10 months	14 months	CBD 600 mg (24 mg/kg/day) PO TID; CBD therapy started after radiation – taken until passing

1436